Ionized Cluster Beams: Physics and Technology

Jpn. J. Appl. Phys. Vol. 32 (1993) pp. 2121–2141
Part 1, No. 5A, May 1993

Invited Review Paper

Ionized Cluster Beams: Physics and Technology

Isao YAMADA and Gikan H. TAKAOKA
Ion Beam Engineering Experimental Laboratory, Kyoto University, Sakyo, Kyoto 606-01

(Received June 20, 1992; accepted for publication March 13, 1993)

Ionized cluster beam (ICB) deposition has been used to form thin films of metals, insulators, semiconductors and organic materials which have unique characteristics when compared to films formed using other techniques. In addition, the use of gas-phase atoms in the form of accelerated clusters has recently shown promise for surface modification applications. A fundamental understanding of ICB deposition and related techniques requires investigations of (1) the mechanisms which lead to the growth of large vapor phase clusters, (2) techniques for determining the size distribution of large vapor clusters, (3) the initial stages of film nucleation, (4) film growth morphology related to lattice mismatch and ion beam parameters. Clarification of the role of clusters in ICB deposition has been greatly aided by atomic scale imaging by transmission electron microscopy and scanning tunnel microscopy in the early stages of film growth. Emphasis is given to the formation of high-quality, epitaxial metallic films. Several applications of ICB films with respect to microelectronics, optical mirrors, compound materials and organic materials are discussed with emphasis on the special characteristics of ICB films. Applications for gas-cluster processing are reviewed.

KEYWORDS: cluster, ionized cluster beam, deposition, epitaxy, migration, large misfit, surface modification, electron device, optical device

1. Introduction

Cluster beam formation was first observed in 1951 during a study of intense molecular beams produced at low temperatures.[1] Becker *et al.*[2] found that a beam composed of clusters of atoms could be formed in the supersonic expansion region of a nozzle flow. Ionized cluster beams from gases were initially applied for fuel injection into thermonuclear plasmas. The cluster beams reduced space charge problems and therefore could be injected into the plasma through a strong magnetic wall. The beams produced were intense with comparatively low energy-per-atom values.[3] Since the energy of the accelerated clusters was too small for useful applications for fuel injection into thermonuclear plasmas, cluster beams were not used in technological fields until those from solid materials were explored as a thinfilm deposition technique.[4] Ionized cluster beam (ICB) techniques for thin-film deposition were first developed at Kyoto University in 1972[5] and subsequently several applications have been scaled up for industrial use. The physical properties of clusters, which consist of two to several hundred atoms, are not the same as those of either liquids or gases. Clusters represent instead a new form of matter. Cluster beams are useful tools for the investigation of the fundamentals of solid-state physics, chemistry and related materials science.[6] This study opens up a new field of materials science which bridges the gap between individual atoms and condensed matter.

ICB techniques have been developed in two important application fields. One is film deposition by ICB from solid-phase materials and the other is surface modification by gas-phase materials. Figure 1 shows an illustration of an ICB deposition system. In ICB deposition, the material to be deposited is contained in a crucible with a small nozzle. The crucible is heated to raise the vapor pressure of the material to several Torr or even tens of Torr. The material escaping through the nozzle undergoes adiabatic, supersonic expansion and a fraction of the atoms condenses into clusters. Clusters generated in this fashion are quite large, containing 200–1000 loosely bound atoms. A fraction of the vapor stream is subsequently ionized by electron impact and accelerated to a few kV to bombard a substrate for the growth of thin films. In the original ICB deposition method, effective use was made of beams of singly ionized clusters containing 10^2–10^3 atoms, in which the constituent atoms had a kinetic energy of the order of a few eV.

ICB depositions have been carried out with a wide variety of materials: metals, intermetallic compounds, semiconductors, oxides, nitrides, fluorides, and organic materials. A principal characteristic of ICB deposition is that high-quality thin films are formed at low substrate temperatures. In many cases, films deposited by ICB have superior density, adhesion, smoothness and crystallinity, electrical characteristics,

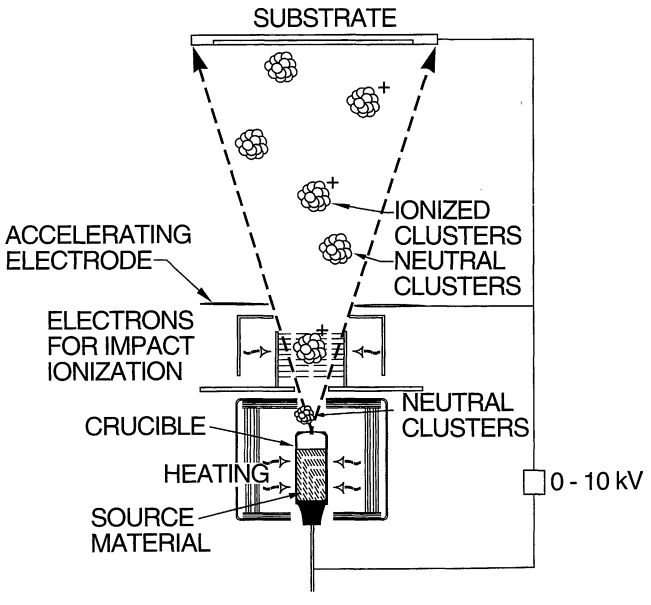

Fig. 1. Schematic diagram of the ICB deposition apparatus.

etc., as compared with films deposited by conventional evaporation or sputtering techniques. An early dramatic example of ICB applications is the low-temperature deposition of epitaxial films on substrates having a large lattice mismatch, *e.g.*, growth of Al on Si.[7] The possibility of forming other epitaxial films on large lattice mismatch substrates has subsequently been investigated. The epitaxial growth of metal and ceramic films (Al, Au, Cu, Al_2O_3, TiO_2 etc.) on various substrates (Si(100), Si(111), Ge(111), Al_2O_3(0001), CaF_2(111), GaAs(100)), and the formation of epitaxial multilayers ($Si/Al/Al_2O_3$, $Al_2O_3/Al/Al_2O_3$) have been studied.[8]

Metal films formed using ICB methods have been found to have extraordinary atomic smoothness, and to exhibit relatively defect-free electrical characteristics. Applications of these novel deposition techniques include formation of high-performance contacts and metallization for advanced integrated circuit (IC) devices,[9] and high-reflectivity mirrors for soft X-ray optical systems[10] and excimer lasers.[11]

Gas-source ICB for surface modification has also been developed.[12] In this case, the cluster material is not necessarily deposited on the surface but provides a high energy-density bombardment and offers many possibilities for new and unique applications in surface processing. The gas-source cluster beams can be used in sputtering and chemical etching of the substrate material, for making surfaces smooth, for shallow implantation of cluster material, and for cluster-activated chemical deposition.

In this paper, we review the recent progress and status of ICB techniques for deposition and surface modification.

2. Calculations and Measurements of Cluster Sizes in Supersonic Expansion Vapors of Metals

2.1 *Formation mechanism of large clusters during supersonic expansion*

Although it is well established that large clusters of gas atoms can be created by condensation of supersaturated vapor produced by adiabatic gaseous expansion through a small nozzle into vacuum, the formation of clusters from metallic vapors is not as well understood. We have shown that a supersonic metallic vapor is produced simply by heating the material to a sufficient temperature so that its vapor pressure is high enough to result in so-called pure vapor expansion through a suitable nozzle.

Figure 2 shows translational velocities determined from time-of-flight (TOF) measurements on free jets of Ag vapor at various source temperatures.[13] The dashed lines show various values of the translational velocity u attained in isentropic (thermal equilibrium) expansions at various values of Mach number M given as

$$u=(\gamma kT_0/m[(\gamma-1)/2+M^{-2}])^{1/2}, \quad (1)$$

where the Mach number is the ratio of translational velocity to sound velocity, γ is the ratio of specific heats at constant pressure and volume (equals 5/3 for a monoatomic vapor), k and T_0 are Boltzmann's constant and the source temperature respectively, and m is the mass of a vaporized atom. In every case, the ejected vapor attained supersonic translational velocities. The corresponding Mach numbers of the vapor increased with increasing source temperature. Moreover, as the nozzle size increased, the velocity also increased, indicating the enhanced conversion of thermal energy to streaming kinetic energy as expected for gas expansion.[14] Figure 3 shows the translational temperature (effective temperature of the vapor atoms along the direction of the jet) in the free jets of Ag vapor as determined from the distribution of the translational velocities. In every case, it was much lower than the source temperature and decreased as the nozzle diameter and source temperature increased, showing the expected increase in Mach number with increasing source nozzle size. These results clearly indicate the occurrence of supersonic expansion which should lead to high degrees of supersaturation in view of the fact that the source vapor is initially saturated. Similar velocity analysis of Ag atoms evaporating from an open crucible, i.e., Langmuir evaporation, indicated that the translational temperature was nearly equal to the crucible (source) temperature and thus demonstrated the absence of any gas dynamic expansion.

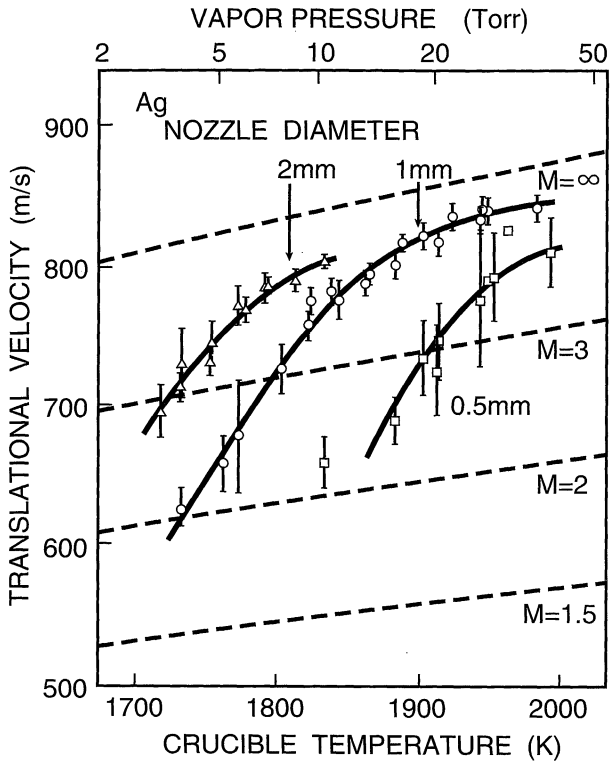

Fig. 2. Translational velocity of Ag clusters measured using the time-of-flight method. The broken lines indicate translational velocities attained in isentropic expansions at the Mach numbers indicated.

2.2 *Simple calculation of cluster size in supersonic vapors*

We have employed the standard theory of homogeneous nucleation to the case of metal cluster formation. This approach is valid because of the results shown in Figs. 2 and 3, which show that metallic vapor beams ex-

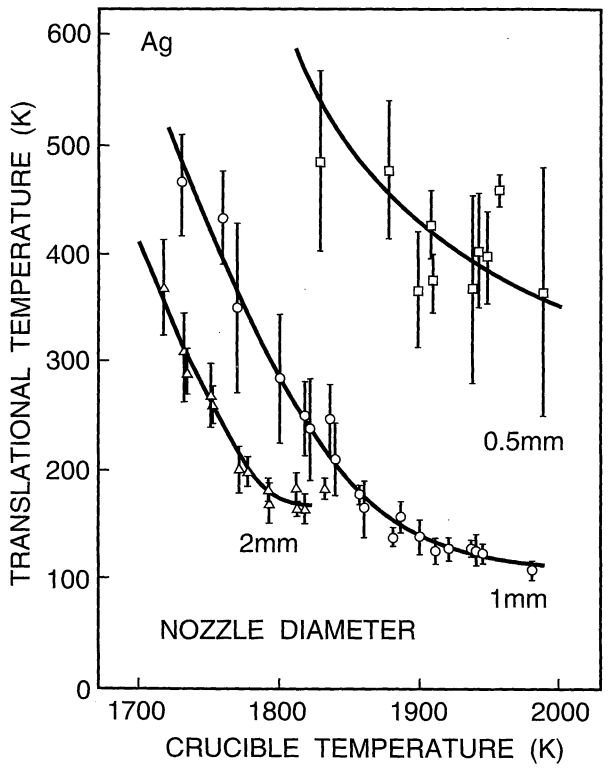

Fig. 3. Translational temperature of Ag clusters measured using the time-of-flight method.

panding through the nozzle have typical supersonic expansion characteristics, resulting in adiabatic cooling. However, according to the discussions of classical nucleation theory by Stein,[15] metals show little tendency to condense due to their high surface tension σ ($\sigma(10^{-3}$ N/m) for Al:865, Ag:957, Ar:13.12 and N:11.77 near the melting temperature).[16] On the other hand, in 1983, we pointed out that the barrier heights and nucleation rates for metals are similar to those of gases in spite of their high σ.[17] This result comes from the fact that the nucleation barrier height is characterized mainly by σ/kT instead of σ alone, where k and T are Boltzmann's constant and temperature, respectively.

Classical nucleation theory shows that the Gibbs free energy change ΔG for the formation of a cluster of radius r is given by

$$\Delta G=-\frac{4}{3}\pi\cdot r^3\cdot(kT/V_c)\cdot\ln S+4\pi\cdot r^2\cdot\sigma, \qquad (2)$$

where V_c is the molecular volume in a cluster, T is the vapor temperature, and S is the saturation ratio P/P_∞ of the vapor pressure P to the equilibrium vapor pressure P_∞. With the assumption of a thermally stable steady state, the nucleation rate J for cluster formation can be expressed by

$$J=\boldsymbol{K}\cdot\exp(-\Delta G^*/kT), \qquad (3)$$

where $\boldsymbol{K}$ is a factor which varies much more slowly with P and T than does the exponential term. Frenkel[18] gave $\boldsymbol{K}$ as

$$\boldsymbol{K}=(P/kT)^2\cdot V_c\cdot(2\sigma/\pi m)^{1/2}. \qquad (4)$$

In addition, ΔG^* is the maximum value of ΔG with respect to r, and from eq. (2), it is given by

$$\Delta G^*=(\Delta G)_{max}=16\pi\sigma^3/3[(kT/V_c)\cdot\ln S]^2. \qquad (5)$$

Since ΔG^* depends on σ raised to the third power in eq. (5) and appears in the exponent of the nucleation rate expression, the value of J is quite sensitive to σ variations. This observation has led to the oversimplified conclusion that materials of high σ are more resistant to the formation of clusters than materials with low σ.[15] The actual situation is, however, more subtle. Figure 4 shows the calculated dimensionless nucleation energy $\Delta G/kT$ that must be overcome to add an atom to a cluster of radius r for several materials. The calculation was made according to eq. (2) by choosing a vapor temperature T_c which gives a supersaturation of $S=100$ (i.e., the vapor pressure in the expanding jet is 100 times the equilibrium vapor pressure at that temperature). We also choose the source pressure to be the typical value of $P_0=10$ Torr. The surface tension of a small droplet is known to be slightly different from the value for a flat plane. However the exact value for a small droplet is not yet known. Therefore, in this calculation, the flat plane value σ_∞ was used. In spite of the high values of σ for metals, it is found that with the exception of Hg, the nucleation energy barriers of metals are not high as compared to gases, because values of σ/kT (10^{19} m^2) are comparable for metals and gases; for example, a value of 6.7 is obtained for Al, 5.6 for Ag, 1.1 for Ar and 1.4 for N. In

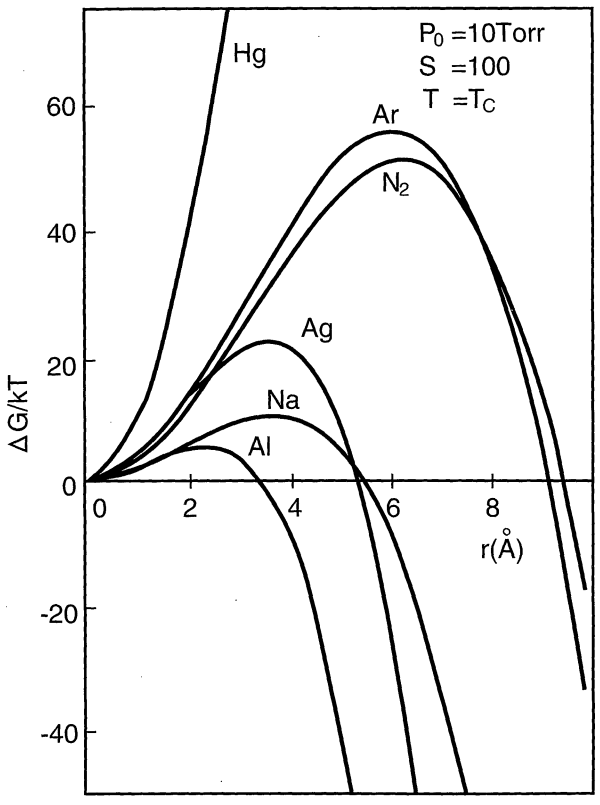

Fig. 4. $\Delta G/kT$ as a function of cluster radius for several materials. (from eq. (2)) The source pressure and the saturation ratio are fixed at $P_0=10$ Torr and $S=100$, respectively. T_c is the vapor temperature which gives a supersaturation of $S=100$.

addition, J is not sensitive to variations of S, because S appears as a logarithmic function in eq. (5).

The formation process for metal clusters during a supersonic nozzle expansion was simulated by combining classical nucleation theory with one-dimensional flow equations. A cluster was assumed to grow from an embryo of critical radius at the maximum value of ΔG. The growth rate, determined by the difference between the rates of impingement and re-evaporation of atoms per unit area, is given by

$$dr/dt=(\xi/\rho_c)(P/(2\pi RT)^{1/2}-P_c/(2\pi RT_c)^{1/2}), \quad (6)$$

where ξ is the sticking coefficient, ρ_c the density of the cluster, T_c the temperature of the cluster, and R is the gas constant. P_c is the saturated vapor pressure at the cluster surface and is given by Thomson's equation[19] as

$$P_c=P_\infty \cdot \exp(2\sigma/\rho_c RT_c r). \quad (7)$$

The one-dimensional flow equations for the conservation of mass, momentum, and energy are given as follows:

$$\frac{d}{dx}\left(\frac{\rho Au}{1-\mu}\right)=0, \quad (8)$$

$$u\frac{du}{dx}+\frac{1-\mu}{\rho}\frac{dP}{dx}=0, \quad (9)$$

and

$$u\frac{du}{dx}+(1-\mu)c_p\frac{dT}{dx}=h_{fg}\frac{d\mu}{dx}. \quad (10)$$

where ρ is the vapor density, A the cross-sectional area of the flow, u the velocity, μ the mass ratio of the condensed phase to the vapor phase, c_p the specific heat of the vapor, h_{fg} the latent heat of condensation and x is the axis along the flow direction. In order to obtain the flow temperature, flow pressure, cluster size distribution and cluster/monomer ratio, these equations were solved using Adams' method.[20] In a typical ICB source, where the vapor is ejected through a short nozzle and is allowed to expand freely, the flow field cannot be described properly by one-dimensional equations such as eqs. (8)–(10). In these calculations, the cross-sectional area of the flow was arbitrarily assumed to be

$$A=\frac{\pi D^2}{4}\left[1+\left(\frac{2x\cdot\tan(\theta/2)}{D}\right)^2\right], \quad (11)$$

where x is zero at the nozzle throat, D is the throat diameter, and θ is the flow divergence angle. D and θ are fixed at 2 mm and 30°, respectively, because our Al film formation experiment showed that the angular distribution of the film thickness deposited using the 2-mm nozzle had a full width at half-maximum of about 30°.

Figure 5 shows the result obtained by solving eqs. (8)–(11) for normalized flow temperature T/T_0 and flow pressure P/P_0 for Al. P_0 and T_0 are the source pressure and source temperature, respectively. As P_0 increases, the promotion of cluster formation is indicated by the increase in the normalized flow temperature relative to the isentropic value (shoulder in Fig. 5). This increase is caused by the release of heat (h_{fg}) during condensation. Figure 6 shows the calculated result of the cluster size distributions for Al at a distance of 6 mm from the throat for different P_0. The cluster size increases with increasing P_0. The simulation shows that the formation of large clusters begins at the upstream position of the throat.

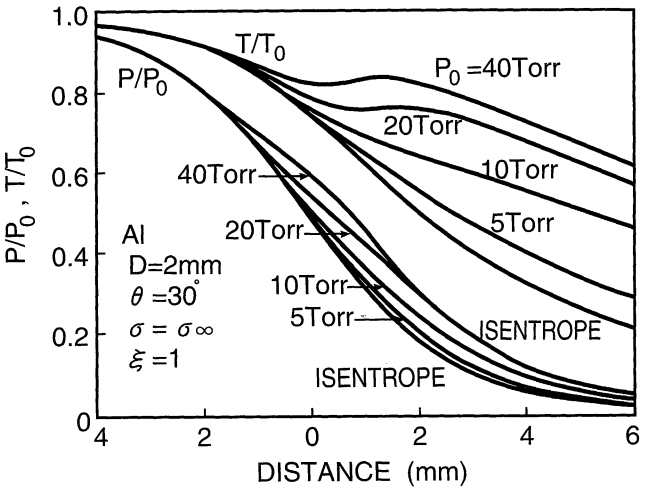

Fig. 5. Variations in the normalized flow temperature T/T_0 and pressure P/P_0 for Al vapor expansion along the flow axis for different source pressures P_0.

Figure 7 shows the calculated variation of mass fraction of clustered material along the flow axis. As expected, this mass fraction increases with increasing P_0. The effects of variation in the values of ξ and σ on cluster formation calculations were also estimated. The change in the cluster/monomer ratio during expansion for different values of ξ and σ was not significant. Since the amount of vapor condensation was insufficient to reduce P significantly along the jet path, neither the vapor flow conditions nor the fraction of clustered material changed markedly along the vapor path.

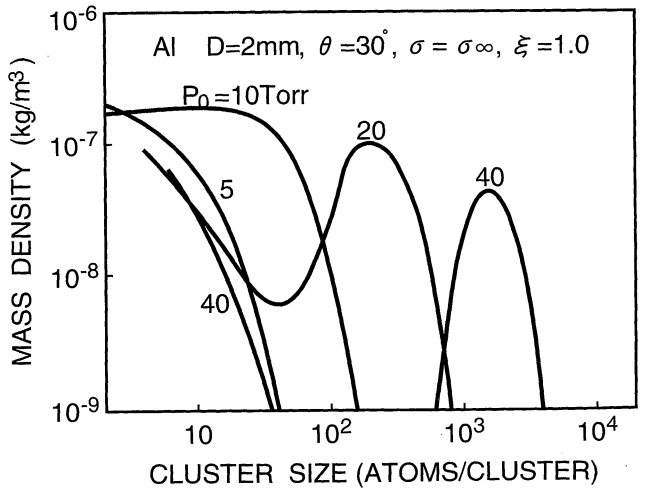

Fig. 6. Cluster size distribution in the Al cluster beam for different source pressures P_0.

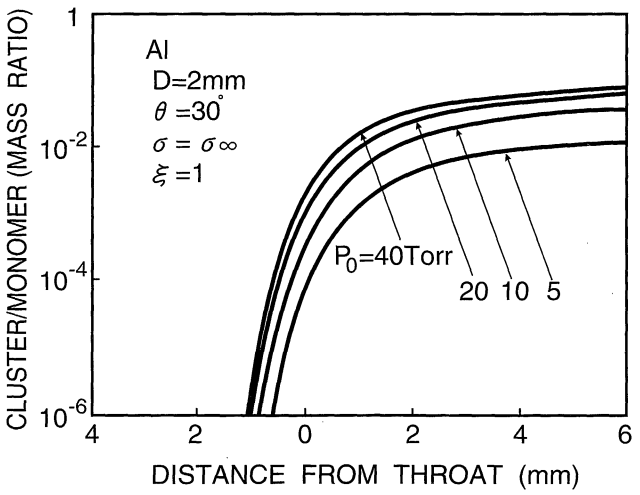

Fig. 7. Mass ratio of clustered material to total irradiated beam, for an Al cluster beam along the flow axis.

Similar calculations have been performed with Ar and other gaseous materials, and compared with the metal vapor results. The results obtained using homogeneous nucleation theory imply that metal vapor is more likely to form clusters compared to gases under comparable expansion conditions. By a rough estimation under practical operation conditions, for example P_0=a few Torr and D=2 mm, large clusters comprise more than a few percent of the mass fraction in the beam.

It is important to note that some metal vapors may contain a considerable proportion of polyatomic species even at thermal equilibrium, while common gases do not. For example, mass spectrometric measurement of ionic species in Ag vapor indicates that more than 70% of the spectrum consists of Ag_2^+, Ag_3^+, and Ag_4^+.[21] This implies that formation of clusters for some materials may start in polyatomic species. This observation implies that clusters are formed more easily in metal vapor than in gases. Although the presence of polyatomic species in metal vapors complicates the theoretical analysis of cluster formation, the above simple treatment provides good insight as to mechanisms of cluster formation.

2.3 *Measurements of cluster size in ICB*

A number of different approaches have been used to determine the cluster size distribution: retarding field measurements,[22-24] TOF mass spectroscopy,[25-29] and transmission electron microscopy (TEM) of low coverage deposits.[30] However, these experiments have failed to provide consistent results for the cluster size distribution and the cluster/monomer ratio. In the following section, recent measurements of cluster size distributions will be shown.

2.3.1 *Retarding potential measurements*

If large clusters aggregate during the expansion from a nozzle, the clusters will have a kinetic energy proportional to the cluster mass. Because all atoms are moving at approximately the same axial velocity due to the supersonic expansion, clusters formed from them must have a similar velocity. These kinetic energies can, at least in principle, be measured by ionizing the clusters and measuring the current on a collecting electrode as a function of the retarding potential. For typical metal vapors at ICB temperatures, the kinetic energy per atom is from 0.1 to 0.2 eV, hence a 1000-atom cluster in a singly charged state will require a retarding potential of 100–200 V to stop its motion. We assume that the cluster ion is singly charged, because doubly and highly charged cluster ions will be broken up by Coulomb repulsion.

Figure 8(a) shows the results for Ga at a crucible temperature of 1670 K, which was obtained by Sosnowski *et al.*[23] A cylindrical nozzle of 1 mm diameter and 4 mm length was used. When the ionizer is turned on, the current decreases rapidly with increasing retarding potential in the negative range. The current in this range is due to the presence of monomer ions. No voltage-dependent current is observed in the positive retarding-potential range, which indicates that there are no large (energetic) clusters in this experimental condition. On the other hand, Fig. 8(b) shows the results at a crucible temperature of 1970 K. In this case, although most of the ions are still monomer ions (hence the current still drops sharply at a retarding potential of almost zero), an appreciable amount of current remains at positive retarding potentials, caused by large cluster ions with high thermal energy. This current decreases gradually with increasing energy, to vanish into the background at 200 V. The cluster size range is estimated by taking into consideration that the atoms emerging from the nozzle have kinetic energy on the order of kT=0.17 eV while the clusters with N atoms have N times that energy. This simple argument indicates a cluster size of up to 1200 atoms with an average size of 100/0.17=600 atoms. This is consistent with the homogeneous nucleation model which predicts generation of large clusters at vapor pressures in the range of tens of Torrs. The total number of atoms in the cluster portion of the beam can be calculated by summation of the atoms for each cluster size. It is estimated from Fig. 8 that the mass flux of the cluster portion is a large fraction of the total flux.

2.3.2 *Time-of-flight (TOF) measurements*

Pulsed electron impact ionization[25-28] and pulsed laser ionization[29] have been used as starting signals in TOF measurements. In a TOF study of Ag from a graphite crucible, excimer laser photoionization was used.[29] ArF laser pulses (193 nm), 15 ns in duration at a repetition rate of 50 Hz were applied for ionization. The acceleration field was oriented normal to the direction of the neutral beam. The crucible, which had a cylindrical nozzle of 1 mm diameter and 1 mm length, was heated in a temperature range of 1700 K to 1950 K, corresponding to Ag vapor pressures of roughly 2 to 30 Torr. After a field-free flight of 20 cm the ions were collected (without multiplication). The amplified current transient was recorded and averaged in a transient digitizer.

The photon energy of ArF laser light (193 nm) is 6.4 eV, which is lower than the ionization energy of Ag

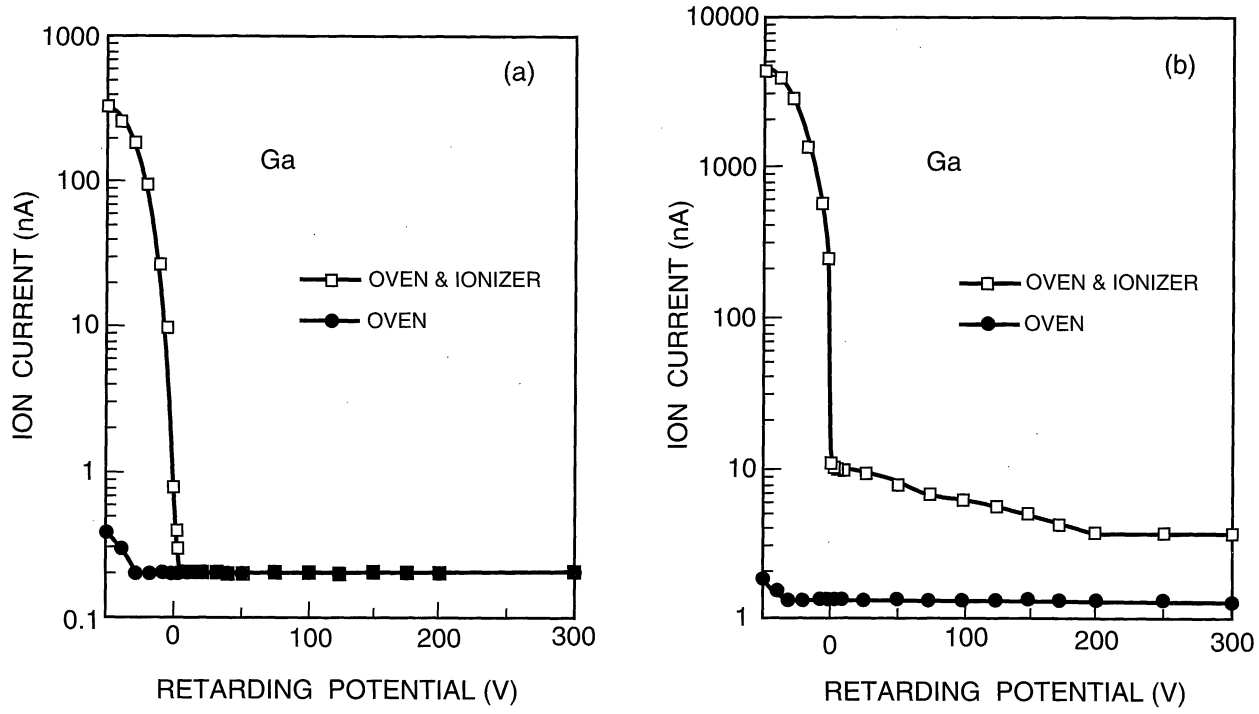

Fig. 8. Retarding potential measurements of current from an ICB Ga source: (a) at 1670 K, (b) at 1970 K. The equilibrium vapor pressures of Ga at these two temperatures are 1.7 and 31 Torr, respectively. Note the change in current scale between (a) and (b).[23]

atoms (7.57 eV), but well above the work function of bulk Ag (4.6 eV), thus increasing the sensitivity for ionization of clusters relative to single atoms. With the assumption that all clusters are ionized and collected, Fig. 9 shows the total number of atoms in clusters in the given ranges of cluster sizes for different deposition rates. The results show that about 0.07% of the Ag atoms coming from the crucible were detected as clusters with more than 25 atoms ($N>25$).

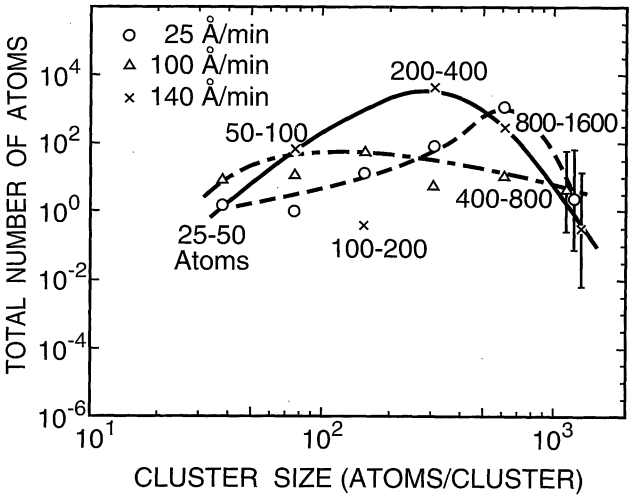

Fig. 9. Total numbers of atoms in clusters with $N>25$ in different ranges of cluster sizes. Each range spans a factor of 2. All atoms in the volume intercepted by the laser are assumed to be totally ionized and collected by the detector.

2.4 *Summary of cluster size determinations*

Calculations of cluster formation during supersonic expansion of metal vapors through suitable nozzles have been performed by combining simple homogeneous nucleation theory with one-dimensional flow equations. The results indicated cluster sizes of up to 1000 atoms, with clusters composing a few percent of the total beam. Retarding potential measurements for Ga cluster beams agreed with these predictions, whereas time-of-flight measurements for Ag cluster beams by pulsed laser ionization gave somewhat smaller cluster sizes and fractions of the total beams.

There are several reasons for uncertainty in cluster size measurements. In many cases, there are problems in cluster detection. The most common method used to detect ions involves the ejection of electrons from a metal surface and amplification by a secondary electron multiplier. However, for efficient detection of clusters, very high kinetic energies must be applied, because the electron yield depends on the amount of energy per atom in the cluster. Therefore, cluster ions which consist of a few hundred to a thousand atoms produce a very small current, even though each cluster ion consists of many atoms. Another problem in the detection of large clusters is that the ionization of the cluster beam by electron impact or laser irradiation can cause fragmentation of the clusters. This fragmentation can be enhanced by the very high temperature of the growing clusters which is caused by the latent heat released by cluster growth during the expansion. The clusters can be cooled by evaporation only after they have entered the high-vacuum region. Gspann estimated a final temperature for the clusters which is much higher than the melting temperature.[31] Although there is no sup-

porting evidence to date, rapid evaporation from large clusters in this high-temperature state might be significantly enhanced by electron bombardment and laser irradiation for ionization. Consequently, in future experiments, the methods for ionization and cluster detection must be carefully considered. We conclude that there is ample evidence for the presence of large metal clusters in supersonic evaporation jets, but that more measurements are required to establish the cluster size distribution.

3. Nucleation and Surface Mobility during Initial Stage of Film Deposition by ICB

3.1 *Nucleation processes*

The early stages of Ag film formation on C substrates have been compared in terms of nozzle source evaporation ("ICB" case) and open source evaporation ("MBE" case), using TEM observations.[30] Surface migration of deposited Ag atoms was suppressed by performing the depositions at 77 K and encapsulating the deposited Ag with evaporated C films prior to warming to room temperature. Figure 10 shows island diameter distributions measured using TEM at 77 K from a nozzle source and an open evaporation source. The average diameter of Ag islands from the nozzle source was approximately 20 Å from the initial exposure until the density of islands increased to the point of coalescence into a continuous film (with average film thickness >2 Å). On the other hand, Ag atoms deposited from the open source crucible formed islands whose average diameter increased steadily throughout the course of the film deposition. Figure 11

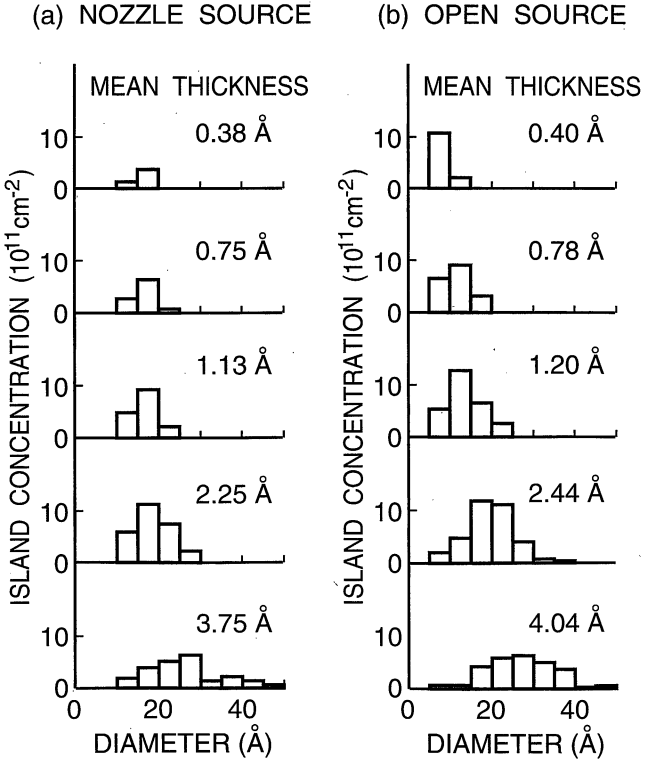

Fig. 10. Island diameter distributions measured by TEM of carbon-encapsulated Ag films deposited at 77 K from (a) a nozzle source and (b) an open evaporation source.

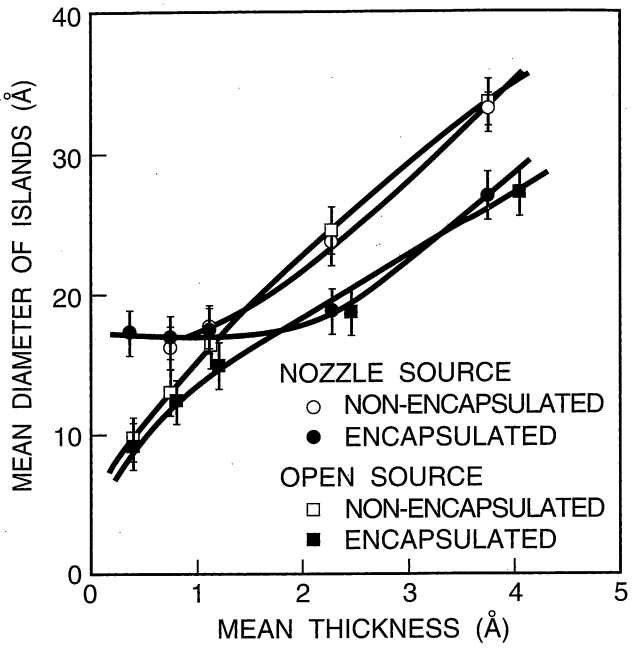

Fig. 11. The mean diameter of Ag islands deposited by a nozzle source and an open source, respectively. Comparison be tween carbon-encapsulated and nonencapsulated samples is shown.

is a plot of the mean diameter of the Ag islands as a function of the mean layer thickness measured from Fig. 10. In the nozzle source case, the mean diameter of the islands was constant at approximately 20 Å at the beginning of the deposition. However, in the open source experiment, the mean diameter of the islands increased continuously. These results suggest that in the nozzle source case film formation started by direct deposition of clusters, and in the evaporation source case, film formation involved nucleation and growth of nuclei from captured migrating adatoms. Experimental results without encapsulation after Ag deposition are also shown in the figure. Since there was no difference between the two cases, the islands were stable over the temperature range of observation.

Similar results were obtained from scanning tunneling microscopy (STM) images of Au atoms deposited on graphite in UHV at room temperature.[32,33] The characteristics of the Au atom beam were controlled by the crucible temperature of the nozzle source. At the crucible temperature of 1920 K, the vapor pressure inside the nozzle source was high enough for the formation of Au atom clusters ("ICB" case) as the beam expanded into the high-vacum region. At the crucible temperature of 1570 K, the Au beam consisted of individual atoms ("MBE" case). Figure 12 shows the results of Au deposition under ICB conditions. The number of Au islands increased with the deposition time and the mean size of the islands remained constant during the early stage of the deposition process. Nucleation sites with random shape were not observed. Moreover, single atoms on the substrate were not observed. Single atoms which bombard the substrate may re-evaporate because they are not stable until they form large embryos greater than the critical size for nucleation. From

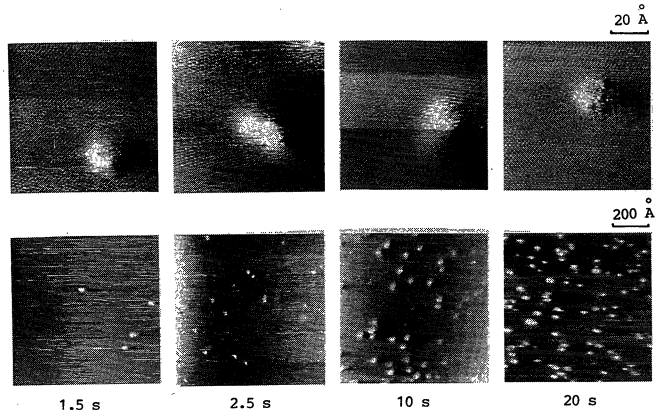

Fig. 12. STM images of gold deposited by the ICB method (source temperature 1920 K, no acceleration) after various deposition times for high magnification (top) and lower magnification (bottom).

Table I. Estimated values of numbers of incident atoms and adsorbed nucleation density for ICB deposition of Au onto graphite. The total number of adsorbed atoms in the nuclei, the sticking coefficient and the ratio of number of clusters to incident atoms are calculated using the above estimated values.

Density of incident atoms (1.5 s)	3.5×10^{14} atoms/cm^2
Nuclear density (1.5 s)	7.8×10^{10}/cm^2
Density of adsorbed Au atoms (1.5 s)	1.4×10^{13} atoms/cm^2
Adsorption possibility $\left(=\frac{\text{Density of adsorbed atoms}}{\text{Density of incident atoms}}\right)$	4.0%
$\frac{\text{Density of clusters}}{\text{Density of incident atoms}}$	0.02%

the STM image of films deposited by a neutral ICB beam, information on the probability of island formation was obtained, as shown in Table I. For the deposition time of 1.5 s, the density of nuclei obtained from the STM image was 7.8×10^{10}/cm^2. Therefore, the density of adsorbed Au atoms was calculated to be approximately 1.4×10^{13} atoms/cm^2, assuming that an island contained approximately 180 atoms, estimated from the island diameter for hemispherical islands.[34] On the other hand, the density of incident Au atoms is about 3.5×10^{14} atoms/cm^2 for a deposition rate of 0.4 Å/s. From these numbers the initial sticking coefficient is calculated to be 0.04. Since the nucleation density is about 7.8×10^{10}/cm^2 which is a typical value observed in films formed using various deposition methods, the ratio of the number of nuclei (equal to the number of clusters) to the number of incident atoms is 0.02%.

A comparison between ICB and MBE depositions was performed using higher-resolution STM observation, as shown in Figs. 13(a)–13(c). For the ICB conditions, nearly hemispherical Au islands were found on the graphite surfaces as shown in Fig. 13(a), even for the briefest beam exposure times. The island diameter was approximately 20 Å, comparable to the TEM results for Ag shown in Fig. 11. For accelerated beam deposition, the Au islands were broken up and consequently were well oriented to the structure of highly oriented pyrolitic graphite (HOPG) substrates as shown in Fig. 13(b). These well-oriented islands lead to the epitaxial growth of ICB films.

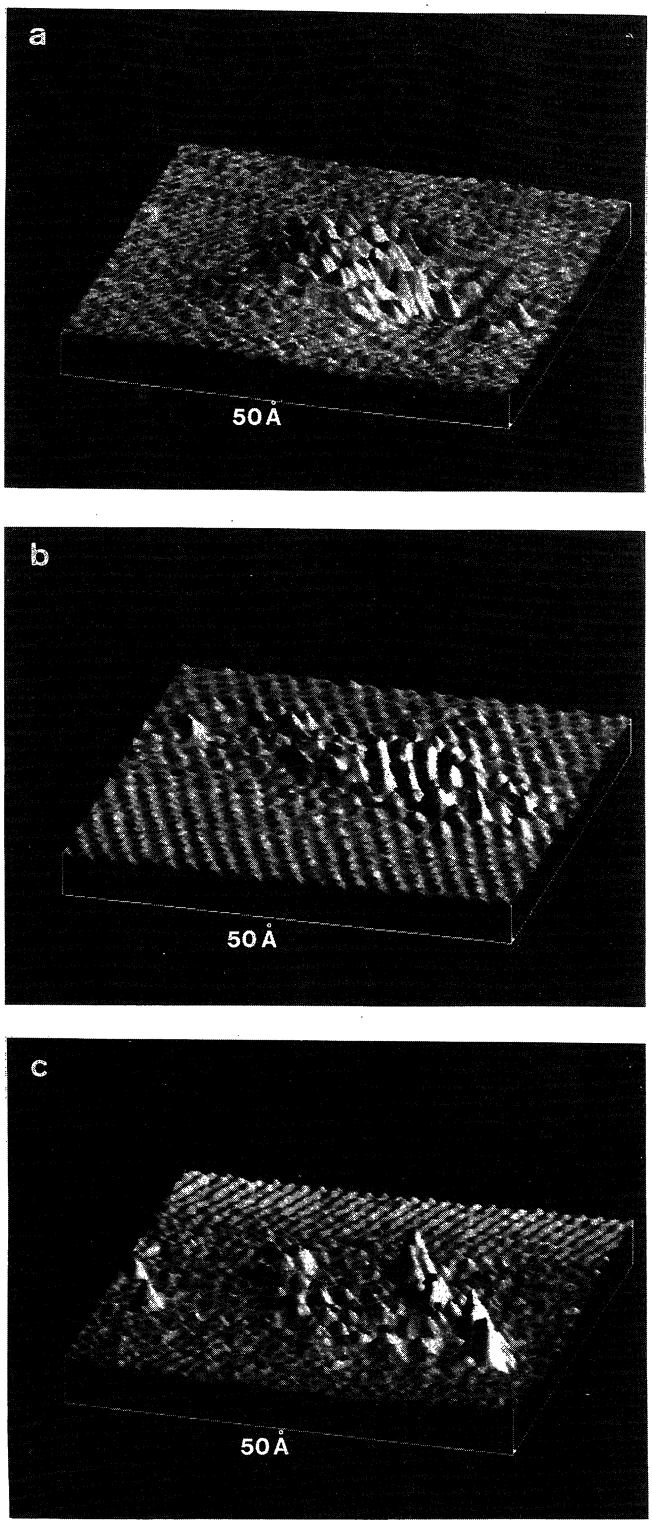

Fig. 13. Comparison between neutral ICB and MBE deposits of Au at the initial stage of the nucleation process. STM images show Au islands formed by (a) neutral ICB, (b) ICB at 3 kV, and (c) MBE.

In the STM images of the MBE deposition, it was difficult to locate any atomic-scale nucleation sites on the substrate after short exposure to the beam. The creation of atomic-scale embryos at the initial stage of

nucleation required at least a few minutes because of significant re-evaporation. As shown in Fig. 13(c), many small nuclei of random sizes were found, but large, round islands such as those of Fig. 13(a) were not observed. Comparison between the ICB and MBE cases suggest that, in the case of ICB, islands were formed by the direct deposition of clusters. It was also found that even for a small fraction of clusters in the beam, the island formation process was significantly altered.

STM analysis of the early stages of ICB deposition of Au on graphite shows that a metal film is nucleated in the form of "instant islands" by cluster impact. However, the film growth characteristics differ greatly, depending on the cohesiveness and mobility of the atoms in the cluster. For the case of ICB deposition of Al on Si and SiO_2, large-scale surface migration of adatoms is observed. Measurements of Al migration on Si(111)[35] and various forms of SiO_2[36] have shown strong anisotropic diffusion effects on Si(111) and dependencies on substrate temperature and ICB acceleration voltages.

These dependencies on cluster-substrate parameters have recently been modeled in terms of the cohesive energy of clusters and the properties of the substrate materials. According to Hsieh and Averback,[37] the following explanation is possible. In the case of Au and Ag, because of their large cohesive energy, impinging clusters form island directly with very little surface migration. In contrast, in the case of Al, because of a relatively small cohesive energy, impinging clusters easily break up on the surface of substrates, leading to enhanced surface migration, which will be discussed in the following section. In all these cases, however, the impinging clusters result in the formation of stable nuclei on the substrates.

3.2 *Adatom migration*

Adatom migration on the substrate surface is one of the most important mechanisms for control of film growth. The migration effect helps the adatoms to interact with each other and to form stable nuclei. It also helps to increase the rate of growth and coalescence of islands. Enhanced migration effects have been observed during Al deposition on a partially shadowed SiO_2 substrate.[36] Figure 14 shows the result of the diffusion distance measurements of Al on two kinds of SiO_2. One type of substrate was a high-temperature oxide (HTO) prepared by steam-oxidizing Si wafers at 900°C. The other type of substrate was a low-temperature oxide (LTO) prepared from a plasma source by deposition onto a Si wafer at 425°C. The diffusion distance of Al increases as the acceleration voltage increases at low substrate temperatures. This tendency continues until 200°C; however, by 400°C the trend is reversed, because re-evaporation of migrating atoms at higher substrate temperatures reduces the adatom dwell time on the substrate. As shown in the figure, the surface condition influences the diffusion distance. The HTO surface is extremely smooth compared with the LTO surface, and the diffusion distance on HTO is larger than that on LTO.

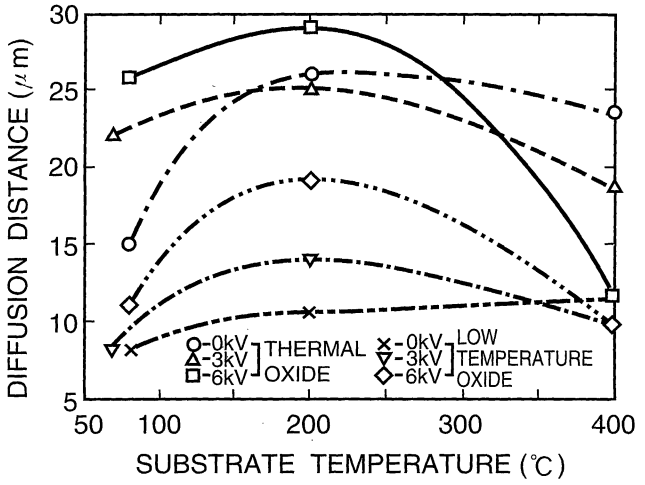

Fig. 14. Surface diffusion distance of Al on two kinds of SiO_2 as a function of ion acceleration voltage and surface temperature.

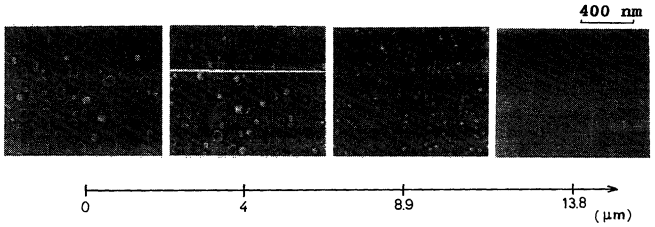

Fig. 15. SEM images of Al crystallites condensed on Si(111) substrate under the mask.

The migration of Al atoms on Si surfaces in connection with Al epitaxy on Si substrates has also been studied. ICB depositions of Al on Si(111) substrates were performed through a stainless steel mask slit at the substrate temperature of 400°C.[35] Figure 15 shows the SEM images of Al deposited at the slit and under the slit cover. The size and shape of islands are different at different distances from the mask edge. The Al diffusion distance under the mask was examined using a surface profilometer, SEM observation and Auger electron spectroscopy (AES) line scans across the Al strip deposit. Diffusion distances as large as 13 to 17 μm were obtained even at the substrate temperature of 50°C.

The adatom migration process for ICB deposition was clarified by computer simulations. Figure 16 shows the simulated impact of an Al cluster consisting of 500 atoms accelerated at 5 keV towards a Si(111) surface.[38] In this calculation, we used the Moliére potential and considered three collision events: collision between two moving particles, between a moving atom and a target atom and between a moving atom and an interstitial atom. This simulation shows that the cluster impact results in an increase in the parallel velocity component for Al atoms, and that the enhancement of surface migration is possible.

Müller[39] performed a molecular dynamics simulation of ICB deposition using the pair-wise additive and

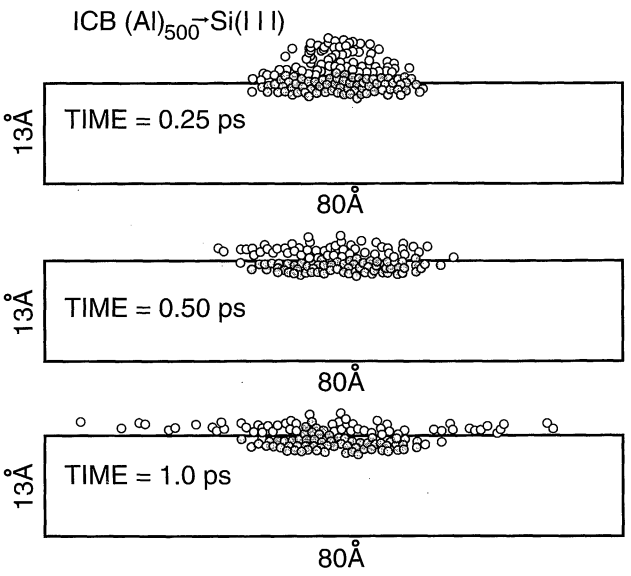

Fig. 16. Simulation of ICB bombardment at t=0.25, 0.5 and 1.0 ps, where a 5 keV Al cluster consisting of 500 atoms impinges on a Si(111) surface.

spherically symmetric Lennard-Jones potential, thus simulating cold clusters. His calculation showed that ionized clusters accelerated above a threshold energy have the potential to form almost defect-free, homoepitaxial thin films, due to impact breakup of the clusters. More recently, Hsieh and Averback[37] examined the collisional dynamics between clusters and substrates using molecular-dynamics computer simulations.

3.3 *Summary of ICB film nucleation and surface mobility*

TEM and STM observations of nuclei formed during ICB deposition of Ag and Au show that clusters of about 20 Å diameter are deposited directly, in contrast to conventional evaporation, where smaller nuclei are formed before growth. At higher cluster beam energies, the deposited clusters break up, causing improved epitaxy. In the case of ICB deposition of Al, the clusters break up on impact (because of the smaller cohesive energy of Al), causing enhanced surface migration of Al atoms. This enhanced surface mobility is important for the growth of smooth epitaxial films. These results show that film growth is affected greatly by the properties of the deposited clusters, such as cohesive energy, cluster temperature, surface tension and kinetic energy. Interactions with the substrate are also clearly important, as will be discussed in §4.

4. Interface Formation and Epitaxy

4.1 *Interface effects*

The initial deposition stage plays an important role in the formation of an interface. An *in-situ* X-ray photoemission spectroscopy (XPS) analysis of the interface characteristics was conducted during the ICB deposition of thin Au films on Si substrates.[40] Although the formation of a stable Au/Si interface is known to be very difficult,[41] ICB bombardment is expected to have a marked influence on the interface characteristics.

Figure 17 shows a comparison of the core level shifts of Si 2p and Au 4f XPS peaks as a function of Au coverage for different ion acceleration voltages V_a. The Au 4f peak shifts towards lower binding energies with increasing Au coverage, while the Si 2p peak shifts towards higher binding energies. In the case of no ionization and no acceleration of the beam (neutral) this trend is in agreement with the results reported from conventional evaporation experiments,[42] and is explained as Au–Si interaction in the initial stage of film formation. When an acceleration voltage V_a was applied at 3 kV, on the other hand, the Si 2p signal showed a negligible peak shift at relatively low Au coverage. This shows that silicide formation was suppressed during Au deposition on the Si surface under this condition. The Au 4f peak approached the bulk value more quickly. It is not understood why the 3 keV energy causes these particular effects. Figure 18 shows

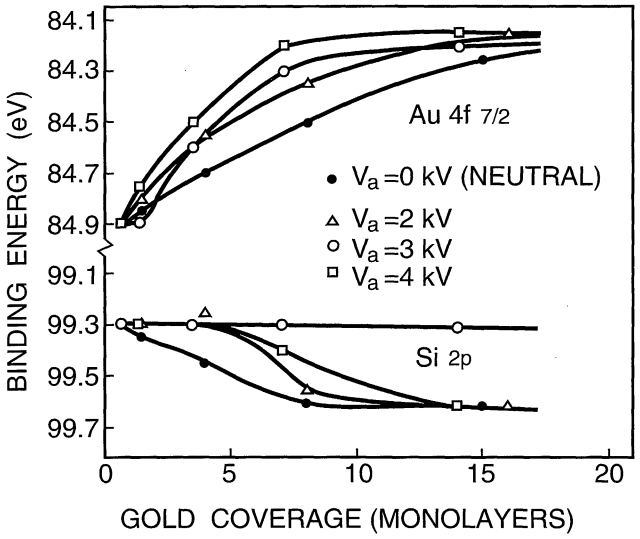

Fig. 17. Si 2p and Au 4f core level shifts plotted as a function of Au coverage on Si for different ICB acceleration voltages.

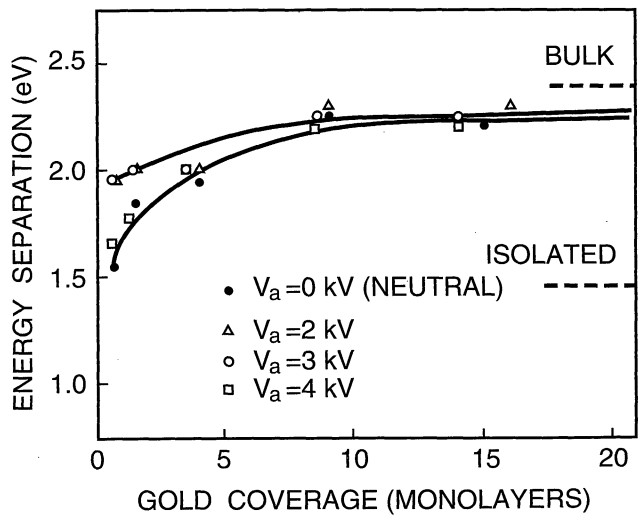

Fig. 18. Energy separation between two main peaks of the Au 5d state.

the energy separation between the two Au 5d peaks as a function of Au coverage. The energy separation of the films deposited at V_a=0 kV indicates that Au is in an almost isolated state up to about one monolayer of coverage. With application of an acceleration voltage at V_a=2–3 kV, however, the energy separation is closer to the metallic bulk value at one monolayer. These results suggest that the film-substrate interaction is suppressed and film formation in ICB is initiated by a metallic-bonding (cluster) deposit, because the interface is stable.

4.2 *Growth morphology*

Due to enhanced nucleation and adatom migration, ICB permits the formation of unique epitaxial films. For example, single crystal Al films are formed on Si, in spite of a lattice mismatch of 25%. Our detailed analysis showed that the Al films exhibit three-dimensional growth during the initial stage. The crystal orientations at this stage are as follows:

Al(100)//Si(111), Al[011]//Si[$\bar{2}$11] denoted as Al(100),

Al(100)//Si(111), Al[011]//Si[$\bar{1}$10] denoted as Al(100)′,

and

Al(100)//Si(111), Al[011]//Si[$\bar{1}2\bar{1}$] denoted as Al(100)″.

That is, Al(100) planes grow on Si(111) surfaces with the Al[011] axis parallel to the Si[$\bar{2}$11] axis, the Si[$\bar{1}$10] axis, or the Si[$\bar{1}2\bar{1}$] axis.

As the deposition proceeds, growth of the Al film becomes two-dimensional with Al(111) planes parallel to the Si(111) substrate surface. The film growth process was studied by *in-situ* AES and *ex-situ* SEM observations. Figure 19 shows the ratio of peak-to-peak intensities of the Auger signals corresponding to Al_{KLL} (1396 eV) and Al_{LVV} (68 eV) transitions as a function of deposition time for Al films grown at room temperature. Due to the greater escape depth for the KLL Auger electrons, the signal ratio indicates whether the growth morphology at the initial deposition was three-dimensional or layer-by-layer. The result shows that layer-by-layer growth is enhanced with increases in the acceleration voltage.

During the later growth stages of Al films deposited on Si(111) substrates by ICB, transmission electron diffraction (TED) and reflective high-energy electron diffraction (RHEED) studies have shown that the Al films grow epitaxially with the following orientation:

Al(111)//Si(111), Al[$\bar{1}$10]//Si[$\bar{1}$10].

This layer-by-layer growth strongly influences the resultant film structure.[43] Figure 20 shows TEM images of Al films deposited at different acceleration voltages V_a. As shown in Figs. 20(c) and 20(d), the number of boundaries and dislocations decreases with increasing V_a. The grain boundaries that are seen as Moiére patterns in Fig. 20(d) indicate low angle grain boundaries. The neighboring grains have a small misorientation of around 1° with respect to each other. (These boundaries are markedly different from the grain boundaries in polycrystalline films, which contain sharp straight-line boundaries with triple points.) These boundaries vanished completely after annealing of the film at 400°C for 30 min in vacuum, and an almost perfect single crystal Al(111) film was obtained.

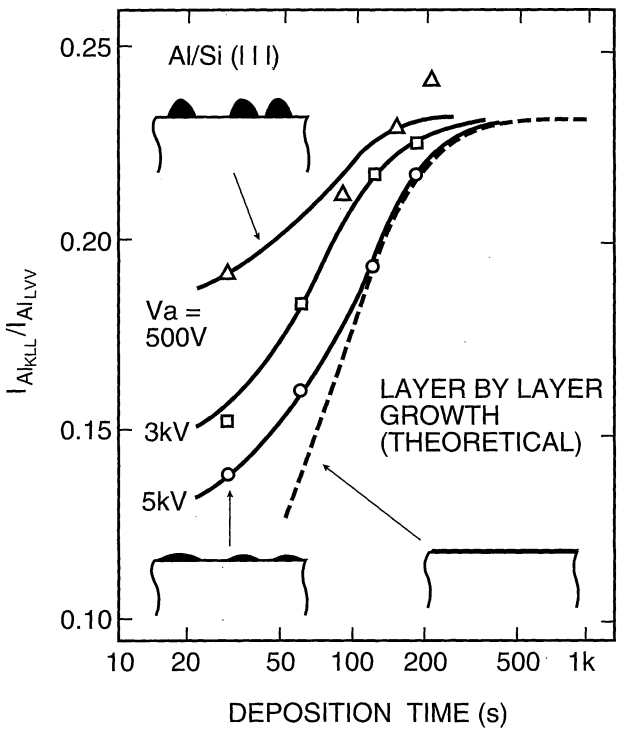

Fig. 19. Ratio of Al_{KLL} to Al_{LVV} Auger signal peak intensity shown as a function of deposition time for ICB films.

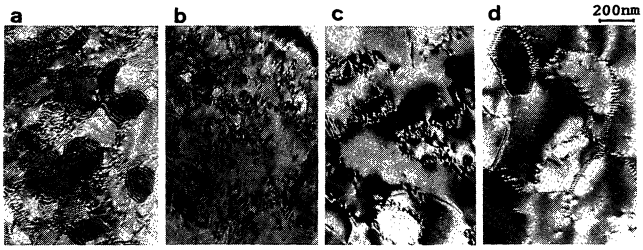

Fig. 20. TEM images of Al films deposited on Si(111) by ICB at different acceleration voltages. The films were deposited at acceleration voltages of (a) 0 (neutral), (b) 1 kV, (c) 3 kV and (d) 5 kV. The marker indicates 200 nm.

Figure 21 shows a cross-sectional image of the Al/Si(111) interface taken at the National Center for Electron Microscopy at the Lawrence Berkeley Laboratory. No damage due to ICB bombardment is seen at the interface. Moreover, lattice distortion near the interface occurs over only a small number of atomic layers. It is seen from this figure that the epitaxial growth is perfect, with four Al interatomic spacings matching every three Si interatomic spacings (a_{Al}=2.86 Å, a_{Si}=3.84 Å). No dislocations are seen for this lattice accommodation. These results show that stable and abrupt junctions are created using epitaxial ICB films. In the case of vacuum-deposited Al films, the interface exhibited triangular pits caused by alloy penetration.[44] AES

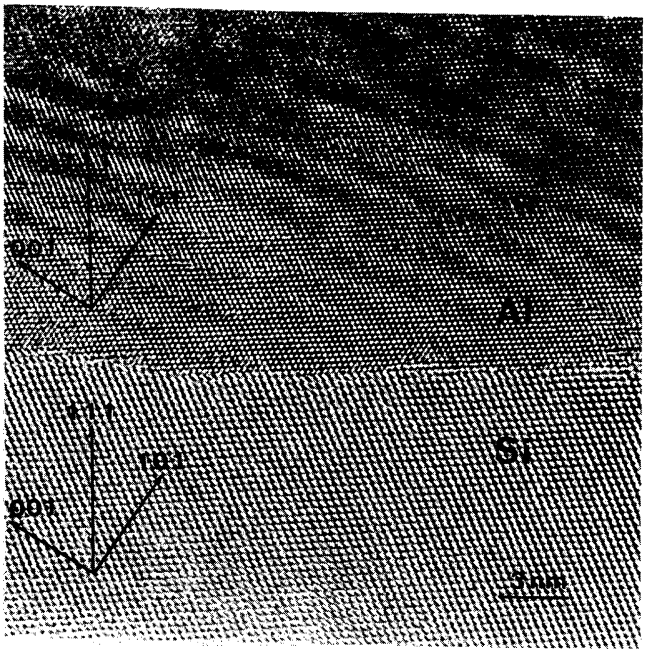

Fig. 21. Cross-sectional TEM image of the interface of an Al film deposited on Si(111) by ICB.

depth profiling of the Al/Si interfaces also showed that the film deposited by ICB has a sharper interface.[45]

In contrast to the Al films on Si(111), those deposited on Si(100) substrates by ICB have a bicrystal structure described by the following epitaxial relationships:

Al(110)//Si(100), Al[001]//Si[011] denoted as Al(110)

and

Al(110)//Si(100), Al[$\bar{1}$10]//Si[011]

denoted as Al(110)R.

The two Al crystals are rotated 90° relative to each other. Figure 22 shows TEM images of Al films on Si(100). The dark and light areas represent the orthogonal film structures of Al(110) and Al(110)R crystals, respectively. The as-deposited films have grain boundaries with smooth curves in random directions. Upon annealing at 500 °C, the grains become larger and the boundaries become faceted. Figure 23 shows a cross-sectional image of the Al/Si(100) interface. The micrograph exhibits a rigid and undamaged interface, as has been found for Al/Si(111). The bicrystal boundary is almost perpendicular to the Si substrate.

Recently, a high-resolution TEM study at Lawrence Berkeley Laboratory was carried out for Al/Ge films fabricated using ICB.[46] TEM pictures at the Al/Ge interface reveal that the interfaces are relatively flat and there is no evidence indicating atomic interdiffusion between the film and the substrate. Figure 24 is a Moiré

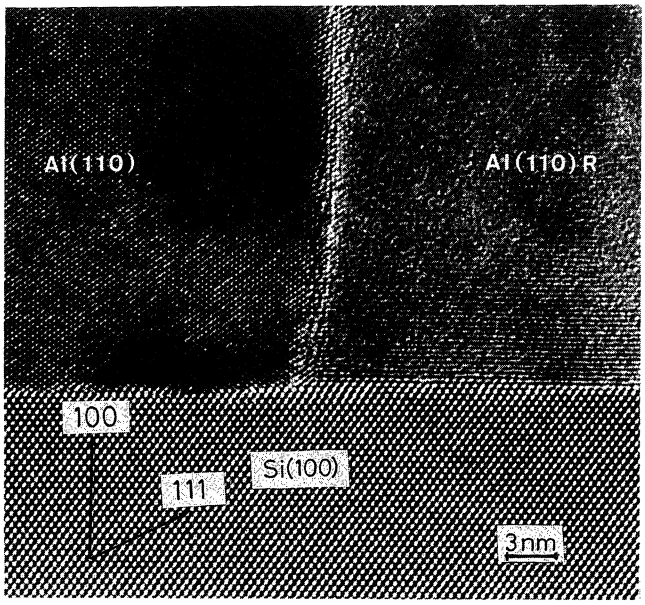

Fig. 23. Cross-sectional TEM view of ICB Al(110)/Si(100) interface.

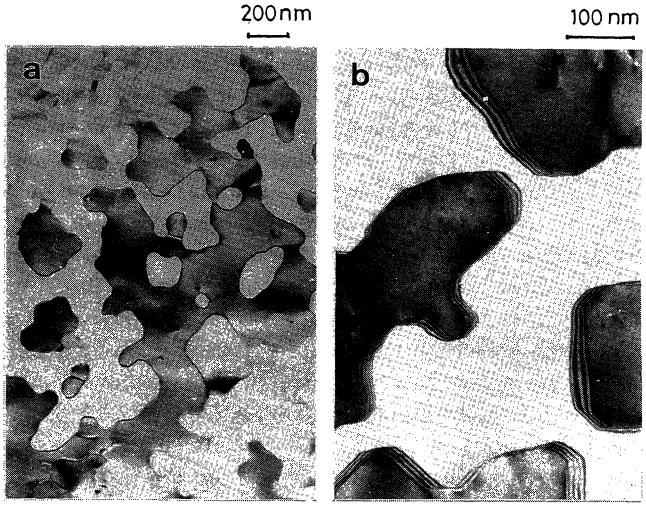

Fig. 22. TEM images of an Al bicrystal film deposited on a Si(100) substrate by ICB. The markers indicate 200 nm for (a), and 100 nm for (b).

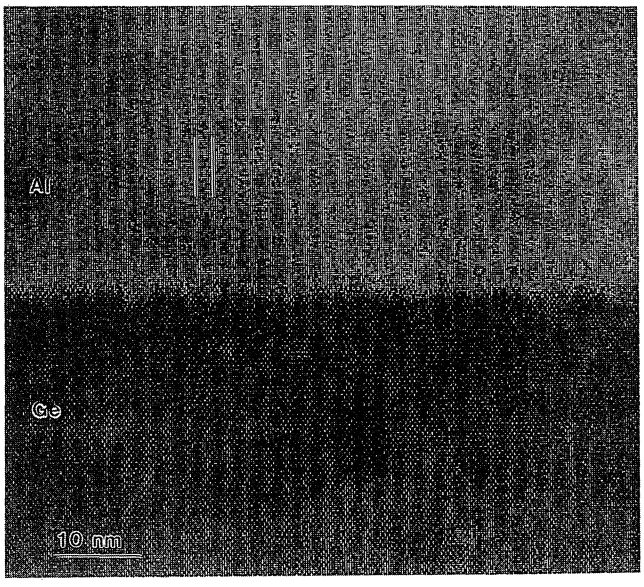

Fig. 24. Moiré pattern produced by superimposing a high-resolution micrograph of the Al/Ge interface with a standard net, indicating the absence of atomic relaxations at the interface. The Moiré period in the Al is indicated.

pattern used to emphasize the pattern of elastic strain distribution. The Moiré analysis shows that there is very little distortion of the pattern in either the Al or Ge lattice, indicating no relaxation of the structure. Figure 25 contains schematic diagrams of (a) rigid and unrelaxed lattices with mismatch, (b) strained lattices, and (c) lattices relaxed into a periodic misfit dislocation array. For epitaxial film growth on different lattice constant materials, the structures shown in Fig. 25(b) or 25(c) are generally formed to release the strain energy at the interface. However, in the case of Al/Si and Al/Ge films obtained by ICB deposition, the films were deposited as a rigid and unrelaxed structure, as seen in Fig. 25(a). A summary of the epitaxial growth of Al on various kinds of substrates is given in Table II, where a is the lattice constant of the substrate, δ the lattice mismatch of Al on various substrates, and Δ the mismatch resulting from the variations in matching invoked to accommodate the lattice mismatch.

Lu *et al.*[47] used a similar deposition method for Al films on Si substrates but emploied a partially ionized beam. During the deposition process, Al ions, which constituted 0.3% of the atom flux, bombarded the surface which was kept at 1 kV. The deposition rate was 10 Å/s. The film was annealed at 450°C for 30 min in an N_2 ambient. The film showed an orientation of Al(110)//Si(110) which was similar to that produced by ICB. Heteroepitaxial deposition of Al on Si has also been studied using electron beam evaporation in a UHV chamber,[48] a CVD method called gas-temperature-controlled CVD,[49] and the bias-sputtering method.[50] Al epitaxial growth, performed using these methods, could not be achieved at room temperature, in contrast to ICB deposition.

Extensive work has been done at the Lawrence Berkeley Laboratory in an attempt to understand the factors that control the film quality and orientation relationship in heteroepitaxial growth. Thangaraj *et al.*[51] studied geometrical models based on the near-coincidence-site lattice (near-CSL) concept as the criterion for heteroepitaxial growth. For parallel epitaxy of Al on Si, the direct mismatch which is calculated from the lattice constant of Al and Si is 25%. However, the near-CSL criterion shows that 3 unit cells in a Si(111) plane are almost equivalent to 4 unit cells in an Al(111) plane. In this comparison there remains only a 0.5% mismatch (Table II). Figure 26 shows a schematic illustration of the near-coincidence site lattice match. The above interpretation could be adopted to explain the epitaxial growth of Al on Si by ICB (see Fig. 21).

4.3 *Summary of epitaxial growth by ICB deposition*

In spite of a 25% lattice mismatch between Al and Si, perfect epitaxial layers of Al can be deposited onto Si(111) by ICB at room temperature. The Al layers are not strained, and the interface is abrupt, in contrast to deposition in other systems and by other deposition techniques. A bicrystal structure was obtained for Al

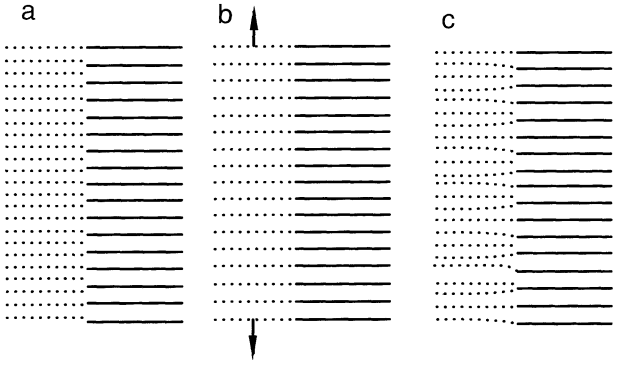

Fig. 25. Schematic illustration of three possible interface structures: (a) rigid, (b) strained and (c) relaxed into a periodic misfit dislocation array.

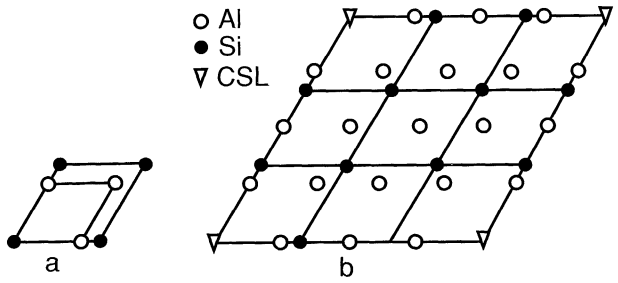

Fig. 26. Superimposed (111) planes of Si and Al where: (a) the direct mismatch between the lattices is 25%; (b) a near-perfect coincidence exists between every 3 Si spac ings and every 4 Al spacings. At the symbol ∇, Al atoms coincide (see also Fig. 21).

Table II. Lattice constant a, crystal structure, and lattice misfit δ of Al films on various substrates. The possible types of matching to accommodate the lattice misfit and the resulting misfit Δ are also indicated for the specified substrate planes. For Al, a=4.049 Å, and the structure is f.c.c.

Substrate	a (Å)	Structure	δ (%)	Plane	Matching	Δ (%)
Si	5.428	Diamond	−25.4	(111) (100)	3:4 match $d_{Al(001)}$ to $d_{Si(011)}$	−0.5 5.5
CaF_2	5.463	Flourite	−25.9	(111) (100)	3:4 match	−1.2
Ge	5.658	Diamond	−28.4	(111) (100)	5:7 match $d_{Al(010)}$ to $d_{Ge(011)}$	0.2 1.2
GaAs	5.653	Zincblende	−28.4	(100)	$d_{Al(010)}$ to $d_{GaAs(011)}$	1.3
Sapphire	4.759	Hexagonal	−14.9	(0001)	Al-to-Al match	4.0

deposited onto Si(100) surfaces. Similar results were obtained for Al deposition onto Ge using ICB.

5. Applications of ICB Films

ICB deposition has been applied to preparation of various kinds of thin-film materials. These include semiconductors, metals, dielectrics, and organic materials. Recent review articles[52] and symposium reports[6,53] have described in detail areas of application and specific film results. Only a few particularly novel applications will be discussed here.

5.1 *Electronic devices*

Progress in the development of VLSI devices has been achieved by a reduction in lithographic dimensions coupled with a corresponding decrease in vertical dimensions. Aluminum metallization has been widely used for contact electrodes and interconnects. However, many problems associated with the electromigration lifetime, contact stability (*e.g.*, junction spiking), corrosion resistance, and multilevel capability have arisen with the reduction in the device size.

The use of single-crystal or epitaxial Al films has been proposed in order to reduce the integration size threshold of VLSI circuits.[54] Figures 27(a) and 27(b) show 100-keV Ga^+ scanning ion micrographs of Al films deposited by ICB and by conventional sputter deposition at the surface and at an intermediate depth (a few monolayers) in the film. The pictures at the intermediate depth were obtained after etching the Al surface by continuous Ga^+ beam exposure. As shown in the figure, with sputter deposition, grain structures could be seen near the film surface and at the intermediate depth, whereas for the epitaxial ICB film, the micrograph is featureless, showing an extremely flat surface with no grain structures. Furthermore, in the micrograph of the intermediate region of the epitaxial Al film, no grain structures could be observed. Figure 27(c) shows etched patterns formed by a scanning Ga ion beam at the middle of the substrate. The micrograph indicates that the etched surface of epitaxial Al is relatively smooth compared to that of the film formed by sputter deposition.

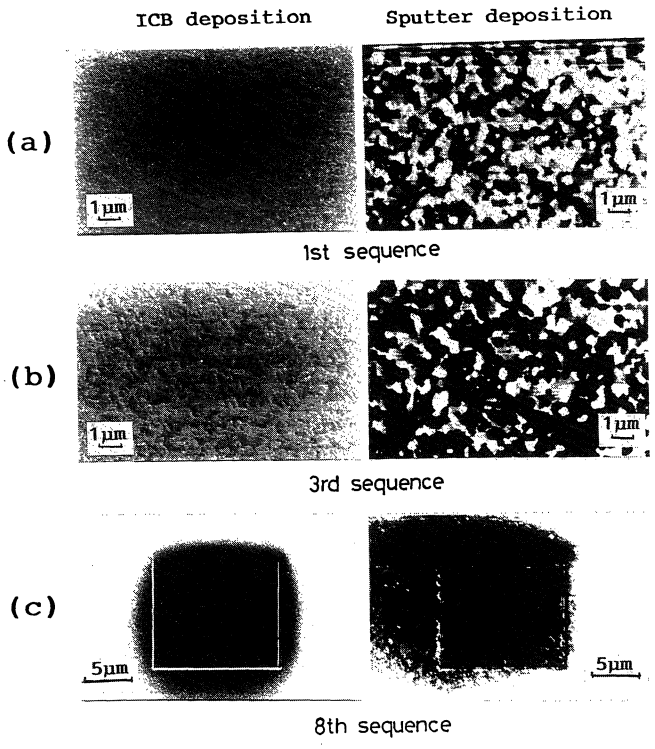

Fig. 27. Scanning ion micrographs (100 keV-Ga^+) of Al films on Si substrate deposited by ICB (left) and by conventional sputtering (right) showing (a) the surface (b) the intermediate region, and (c) a pattern etched by a scanned Ga ion beam.

Epitaxial films are more resistant to heat cycles and to corrosion, because residual chemicals remaining in grain boundaries after etching can be eliminated. Problems related to electromigration and stress migration can also be eliminated because these problems are related to diffusion along the grain boundaries. Several unique characteristics of ICB single or epitaxial Al films are described below.[54]

5.1.1 *Interdiffusion*

It is commonly recognized that in the integrated circuit structure, the diffusion of Si in pure Al films is enhanced by the polycrystalline nature and imperfections of the Al film. For an annealing time of 30 min at the temperature of 550°C, the diffusion length for Si in thin Al film is reported to be 83 μm (diffusion constant: $D=3.5\times10^{-8}$ cm^2/s).[55] The Si solubility at 500°C is about 0.9%. (Auger analysis shows a detection limit of 0.1% for Al in Si.) However, in epitaxial Al films deposited on both Si(111) and Si(100) substrates, detectable amounts of Si could not be seen by AES after annealing at 500°C. Though the Al film on Si(100) was an epitaxial film with two microcrystals, the results were similar to those of single-crystal Al on Si(111) substrates.

5.1.2 *Morphology*

Changes in the morphology of the surface and the interface after annealing at 500°C for 30 min were examined by SEM. No annealing hillocks or valleys are seen on the surface of the epitaxial Al film. At the interface of the sample prepared by conventional vacuum deposition, there are many deep pits and undulations caused by so-called alloy penetration, while no irregularity can be seen at the interface of the ICB-deposited sample.

5.1.3 *Electromigration*

The electromigration in an epitaxial ICB Al(111) film on Si(111) has been tested. A 400-nm-thick Al film was chemically etched onto 10-μm-wide, 1000-μm-long strips. They were stress tested with a current of 10^6 A/cm^2 at 250°C. There was no change in resistance even after 400 h of operation, in contrast to sputtered Al films, which normally fail at 10^6 A/cm^2 after 20 h.[56] The electrical resistivity of 2.7 $\mu\Omega\cdot$cm for the 400-nm-thick film was comparable to the bulk value.

5.1.4 *Contact*

In conventional metallization techniques, recrystallization of Si that has been dissolved in Al causes such problems as an increase in contact resistance and destruction of the junction. Schottky contact characteristics were studied for ICB epitaxial Al films. Al/n-Si(0.7 $\Omega\cdot$cm) junctions of 1 mm diameter were fabricat-

ed and the current density-voltage (J-V) characteristics were measured before and after annealing at 450, 500 and 550°C. Figure 28 shows the change in the Schottky barrier height and ideality factor (n) of the junction. The barrier height and the n value are around 0.73 eV and 1.17, respectively. The barrier height and n value change by 0.03 eV and 0.02, respectively, while in the case of the Al–Si junction fabricated using conventional deposition techniques, changes of more than 0.1 eV and 0.1, respectively, have been reported.[54] It is thought that the dissolution and/or the recrystallization of Si are suppressed in the epitaxial Al films.

An infrared scanning internal-photoemission microscope[57] was used to measure the Schottky barrier height, $q\Phi_B$. The laser beam is transmitted through a single-mode fiber which has a core diameter of 5 μm, collimated by an infrared objective lens and then focused on the Al/Si interface. The advantage of internal photoemission measurements is that they are not affected by ohmic backside contacts and leakage currents around contact areas.

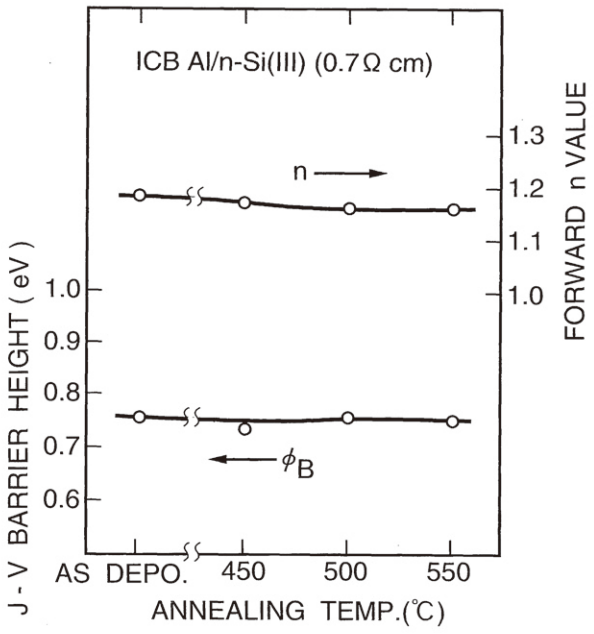

Fig. 28. Schottky barrier height Φ_B and ideality factor n of ICB-Al/n-Si junctions after annealing to successively higher temperatures.

Figure 29 shows the maps of barrier height ($q\Phi_B$) for two types of ICB epitaxial Al (on Si(111) and Si(110)), and vacuum deposited Al on Si(110), measured using infrared scanning internal photoemission microscopy. The Si substrates used are of the n-type, and the resistivity is about 10 Ω·cm. The values of $q\Phi_B$ are different, indicating relatively high values of $q\Phi_B$ for the deposited epitaxial Al contacts. Since the resultant energy accuracy is estimated as 20 meV for the barrier height of 0.8 eV, the difference is larger than the experimental error. The epitaxial Al/Si films show Schottky barrier heights which are greater than those of the conventional depositions (Fig. 29(c)).

The lower value of the Schottky barrier height for the conventional Al–Si contact is due to the interface layer formed on the substrate. Similar results are reported for Cu and Ag, where exposing a cleaved surface to oxygen before evaporation results in a significant decrease in the barrier height. The presence of an oxide layer causes interface defects, i.e., band gap states which pin the Schottky barrier height at the center of the band gap. In contrast, the epitaxial Al film on Si(111) has few interface states caused by defects or interface layers, as shown in the cross-sectional TEM images. The Al films grown on Si(110) may have some interface states caused by defects on the substrate. Thus the finding that the Schottky barrier height of epitaxial Al/Si samples exceeds that of conventional Al/Si samples indicates that reduction in the number of the interface states leads to an increase in the Schottky barrier height.

According to the theory proposed by Mönch,[58] origins of the defect pinning states are classified using two models. One is the virtual gap state (VGS) model. The other is the defect-induced gap state (DIGS) model. This classification is in good agreement with experimental data and reveals clearly that the defects at the interface reduce the Schottky barrier height. However, the value of barrier height obtained from the internal photoemission is relatively high, especially in the case of single-crystal Al films compared with the

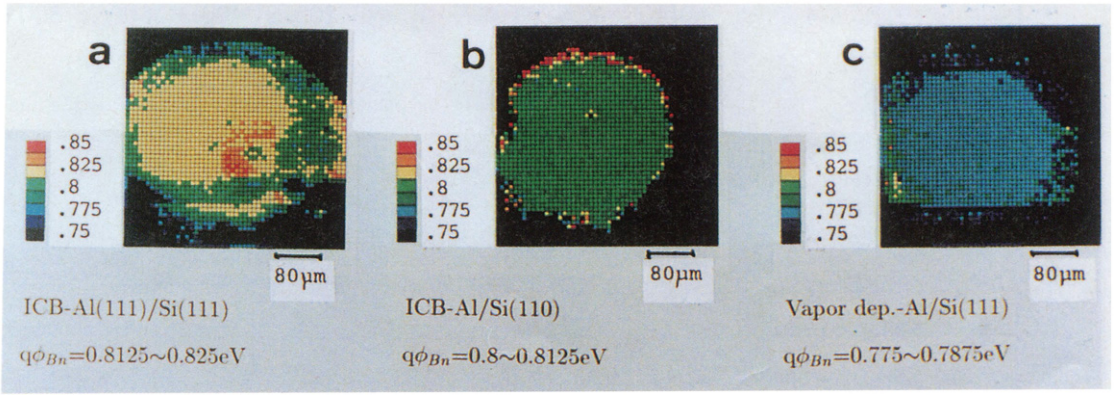

Fig. 29. Maps of Schottky barrier height for three types of epitaxial Al on Si substrates, measured by an infrared scanning internal photoemission microscope. (a) epitax ial Al on Si(111), (b) epitaxial Al on Si(110), and (c) vacuum-deposited Al on Si(111).

previously reported data. The barrier height was also determined by *I-V* and *C-V* measurements.[9] Although inadequacy of the ohmic contacts on the backside of Si prohibited the absolute determination of the Schottky barrier heights obtained using *I-V* and *C-V* properties, it was observed that the barrier height was larger, in the case of the near-ideal Al–Si contacts.

5.2 *Optical devices*

ICB deposition has been applied to the fabrication of films which are suitable for use in X-ray and laser mirrors. By the use of conventional film deposition methods, the films were usually fabricated at low substrate temperatures in order to obtain a flat surface. However, these conventionally prepared films have shown low packing density, poor reflectivity and low threshold damage values.

X-ray mirrors with atomically flat surfaces, and with high reliability and durability have been deposited by ICB in UHV.[10] High-purity (99.99%) Au was charged in a carbon crucible, and heated to 1750–1800°C by electron bombardment. Au beams ejected from the 2 mm nozzle of the crucible were ionized and accelerated to the SiO_2 substrate. The electron current for ionization was kept at 100 mA. The acceleration voltage, V_a was varied from 0 to 5 kV. The deposition rate was kept at 30 Å/min by adjusting the crucible temperature. The film thickness was in the range of 230 to 700 Å. The substrate was kept at room temperature during the deposition. Figure 30 shows the X-ray reflectivity of the Au films deposited at various V_a. The X-ray was $Al_{K\alpha}$ at a wavelength of 8.34 Å. The reflectivity increases with increasing V_a, and the film deposited at V_a=3 kV shows a reflectivity of 95% at the incident angle of 0.75°. This is 10% larger than the value calculated using Fresnel's equation, in which the surface roughness is zero and the optical constants reported by Henke are used.[59] The high reflectivity may originate from the high density and low defect concentration of the films. It should be noted that the spot size of the incident X-rays on the reflecting surface increases with decreasing incident angle. The X-ray reflectivity decreases rapidly at an incident angle less than 0.5° because of the length of the sample. The root mean square roughness was calculated from the X-ray reflectivity as a function of incident angle and the roughness was 2.5 Å.

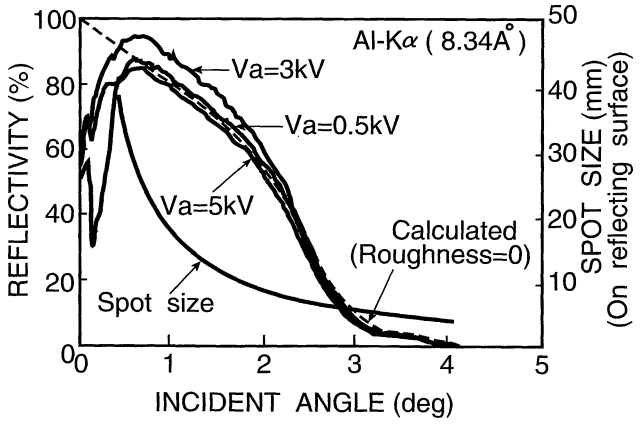

Fig. 30. Dependence of X-ray reflectivity on the incident angle for Au films prepared by ICB at different acceleration voltages. The dotted line shows the values calculated using Fresnel's equation, in which the surface roughness is zero and the optical constants are Henke's values.

An increase in the reflectivity is also observed when the thickness of a very thin film is increased. This is due to improved surface flatness. As shown in Fig. 31 the reflectivity is 88% at a thickness of 230 Å where the incident angle is 1.0°. This value is 8% larger than the calculated value. It also shows that the reflectivity does not decrease with film thickness. Film roughness usually increases as the film thickness increases when a film is deposited using conventional evaporation methods. However, the film deposited by ICB does not show any appreciable increase in the roughness as the film thickness is increased. The Au films prepared by ICB have good surface flatness even at a thickness of 1000 Å.

Epitaxial Al films deposited using ICB on Si(111) substrates have been tested for use in an excimer laser mirror.[11] A steam treatment test shows that the ICB-Al film has excellent resistance against oxidation. Table III lists the reflectance of the epitaxial Al film for various excimer laser wavelengths at different angles of incidence. It should be noted that the epitaxial Al mirror shows only a small change in reflectance with respect

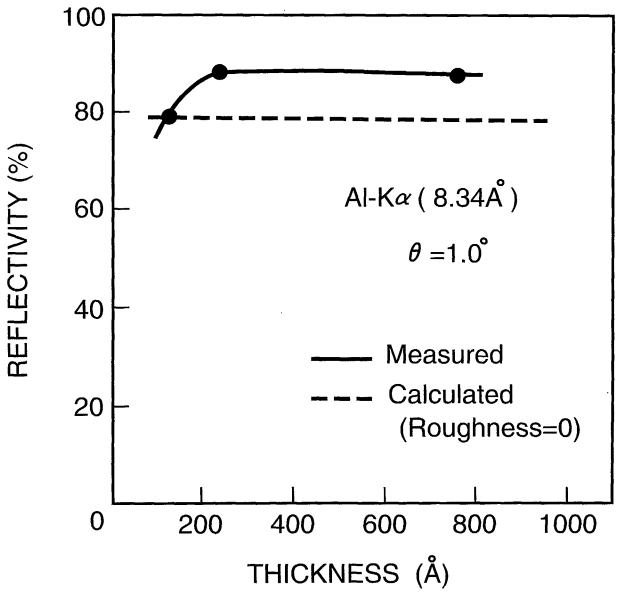

Fig. 31. Dependence of X-ray reflectivity on the film thickness for Au films prepared at an acceleration voltage of 3 kV.

Table III. Values of the reflectance of ICB epitaxial Al films for various excimer laser wavelengths at different angles of incidence.

	Angle of incidence		
	θ=5°	θ=12°	θ=45°
ArF, λ=193 nm	—	79	83
KrF, λ=248 nm	—	92	91
XeCl, λ=308 nm	—	92	89
XeF, λ=351 nm	90	90	87

to the wavelength and the incident angle. These results indicate that an epitaxial Al film shows potential for use in an excimer laser mirror under various optical conditions. The radiation damage resistance of the epitaxial Al film was studied by ArF excimer laser irradiation. The Al film was coated with an MgF_2 protective layer. A focused excimer laser beam was directed at the specimen at an angle of 2° from the normal of the film surface. The laser beam was fired in a series of 1000 pulses which was acoustooptically Q-switched to a pulse width of 20 ns at a frequency of 100 Hz. The shots were fired successively with increasing laser power until damage was detected on the mirror surface. A high threshold value (1.0 J/cm^2) of laser damage was obtained with good reproducibility. This value is considerably higher than that for conventional evaporated Al films and is suitable for practical use. Because the damage appears to occur only in the MgF_2 film, it is expected that laser mirrors of higher performance with a better quality protective layer can be produced using ICB.

5.3 *Other applications*

ICB methods have been used to form thin films of high-temperature superconducting materials, compound and elemental semiconductors, metal oxide: ceramics and organic compounds. Many of these films have unique characteristics, such as high density, high adhesive strength, controlled stress and well-controlled chemical composition. Crystalline films formed using ICB methods also often have unique structure and orientation, including epitaxial alignment even for large lattice mismatches.

Reactive ionized cluster beam (R-ICB) techniques have been used to form thin films of YBCO and EBCO films on $SrTiO_3$ and MgO substrates.[60] In the R-ICB process, metals such as Y, Er, Ba and Cu are evaporated from separate ICB sources and co-deposited in the presence of a local flow of reactive gas, such as O_2 or O_3. Such films have a well-controlled composition, good adhesion and high density. YBCO and EBCO thin films have been obtained with T_c above 84 K and J_c of 1.2×10^6 A/cm^2. These superconducting films have been formed at relatively low temperatures (610°C) and some oriented films have been obtained by R-ICB at temperatures as low as 510°C.

GaAs epitaxial layers can be grown on Si(100) using dual-ICB sources for evaporation of As and Ga.[61] The enhanced nucleation rate of atomic beams containing clusters allows the formation of epitaxial GaAs films on Si at relatively low temperatures. Since the thermal expansion coefficients of GaAs and Si differ by 60%, lower temperature deposition results in films with lower stress, which in turn gives improved IC device performance and lifetimes. GaAs films have been formed using the ICB methods with crystal quality comparable to that of films formed at higher temperatures using the MBE or MOCVD method.

Epitaxial multilayers of metal-oxide insulating materials have been formed by R-ICB on metal and metal-oxide substrates.[62] For example, epitaxial Al_2O_3 films have been grown on Al(111)/Si(111) substrates by combining Al evaporated from an ICB source with a reactive O_2 gas flow directed towards the depositing surface. The Al(111)/Si(111) substrate was itself formed by epitaxial deposition of Al from an ICB source onto Si(111). In spite of the 16.8% lattice mismatch between Al(111) and Al_2O_3, epitaxial Al_2O_3(0001) layers were formed at a substrate temperature of 200°C. In addition, epitaxial films of rutile-TiO_2(200) have been grown on Al_2O_3(0001) at 450°C by combining ICB deposition of Ti with a beam of partially ionized O_2 gas.[63]

Organic thin films deposited using ICB methods often have higher density and better-controlled molecular structure than those formed using plasma-assisted deposition methods. The crystallinity and orientation of many organic films can be controlled to a high degree by appropriate selection of the ICB deposition conditions. Anthracene thin films have been deposited on glass as large-grain crystallites which have preferential orientation of the (001) plane parallel to the substrate.[64] These films also have superior photo- and electroluminescent characteristics.

Chemically active films of porphyrin have been formed by ICB deposition using sublimation-purified tetraphenyl-porphyrin-Fe-chloride.[65] In the ICB deposited films, the Cl coordination is removed which results in a change in the oxidation state of the Fe from +3 in the source material to +2 in the deposited film. The presence of Fe^{+2} complexes in the ICB deposited film is responsible for reversible oxygenation capabilities of the film.

5.4 *Summary of applications for ICB films*

The applications of ICB films are numerous, because these films have greater smoothness, better epitaxial quality and often higher density and adhesion than films grown using other methods. In addition, greater control over the impurity levels can be achieved because of the low growth temperatures. The wide range of applications of ICB films includes the following: (1) Al films deposited by ICB for metallization on VLSI devices are almost free of grain boundaries, leading to marked reductions in electromigration, interdiffusion of Si, corrosion and contact resistance, as well as improved thermal stability with regard to Schottky barriers. (2) Au films for X-ray mirrors have exceptionally high reflectivity (95% at an incident angle of 0.75° and λ=8.34 Å), which is higher than that calculated for a perfectly smooth surface. Al ICB films for excimer laser mirrors show a high resistance to laser damage. (3) Epitaxial multilayers of Al_2O_3/Al/Si and TiO_2(rutile)/Al_2O_3 have been grown at low temperature by ICB. (4) Progress in the formation of ICB films of superconductive YBCO and EBCO and of GaAs epitaxial layers on Si(100) is reported. (5) Organic ICB films of anthracene and porphyrin, with high density and good crystallinity have been grown.

6. Production of Gas Clusters and Applications to Surface Modification

The impact on surfaces of accelerated clusters con-

sisting of gas atoms does not normally lead to the formation of a thick film of these atoms. However, the characteristics of the bombarded surface are significantly altered by the impact of either inert or reactive gas clusters.[12,66] Some applications include surface smoothing by enhanced atomic rearrangement and cleaning by reactive removal of surface contaminants in atomic, molecular or small particle form. Because significant energy in the accelerated gas-cluster beam is delivered to the surface even though the energy-per-atom is low (a few eV), such surface modification techniques are expected to induce less lattice damage and fewer recoil events than atomic ion processes such as sputtering and plasma etching. At somewhat higher beam energies, hypershallow implantation of the gas-cluster atoms is expected. The enormously high atom flux density of an energetic cluster impact can be expected to result in modifications of the initial state of damage, changes in the range of the implanted ions and perhaps suppression of effects such as deep atomic penetration along high-symmetry directions in crystalline targets ("channeling") that limit the effectiveness of low-energy atomic ion beams for the formation of shallow implanted layers.

Gas clusters of considerable size are formed, even at room temperature, by adiabatic expansion from a high-pressure region into a high-vacuum region through a small-bore (0.1 mm) conical nozzle.[66] A beam containing a large fraction of large clusters is obtained by placing a "skimmer" downstream, close to the nozzle and providing high pumping speeds in this region. For the case of CO_2 gas clusters, beams containing clusters with mean sizes of 10^2–10^3 molecules (as measured by the diffraction of a crossbeam of electrons) are obtained in this manner.[12] The mean size of the CO_2 clusters increases with the source line pressure as shown in Fig. 32.

By the use of a retarding potential filter, small ionized clusters and atomic ions can be removed from an ionized gas-cluster beam. Figure 33 shows the change in the refractive index of an amorphous Si surface after bombardment by CO_2 molecular and cluster ions as a function of V_a. The index of refraction of Si after exposure to a dose of 10^{15} ions/cm^2 increases strongly with V_a for the impact of monomer (single-molecule) ions. After exposure of Si to a gas-cluster beam consisting only of CO_2 clusters containing 500 or more molecules, only a slight shift in the index of refraction is observed, with no strong V_a dependence. This result and Rutherford backscattering spectroscopy (RBS) channeling analysis of bombarded Si surfaces indicate that the surface damage created by the impact of a large gas cluster is far less than that created by the impact of a similar number of monomer ions accelerated across the same potential.

In spite of the relatively low levels of surface damage, the impact of accelerated gas clusters can significantly alter the texture of bombarded surfaces.[67] Figure 34 shows the SEM image of a Cu surface bombarded with an Ar cluster beam which had a mean cluster size of 300 molecules and was accelerated across a 30 kV potential drop. The figure shows that

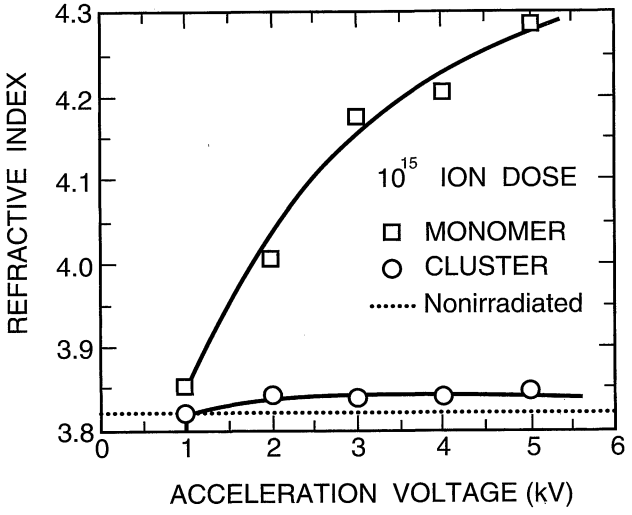

Fig. 33. Refractive index changes in Si surfaces bombarded by CO_2 cluster beams and molecular beams. Clusters with less than 500 molecules/cluster were eliminated.

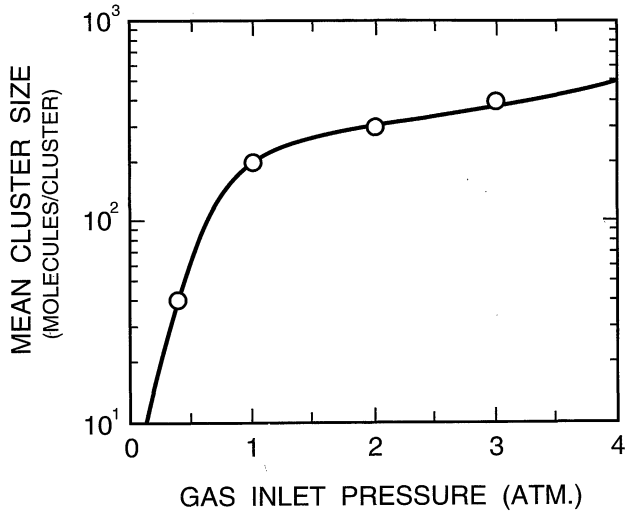

Fig. 32. Mean cluster size distribution as a function of pressure of CO_2 gas introduced to the nozzle. The throat diameter is 0.1 mm and the nozzle length between the throat and outlet is 30 mm.

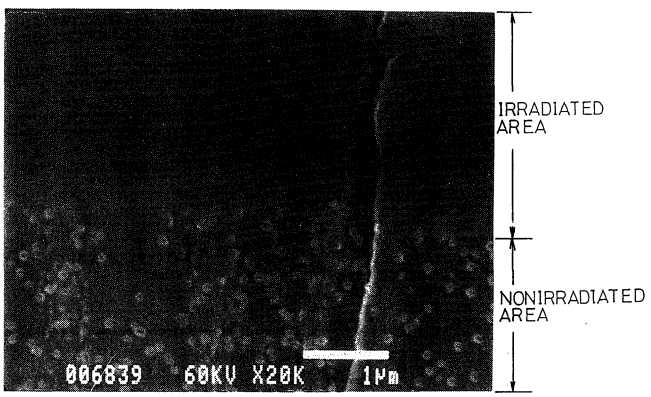

Fig. 34. SEM image of a Cu surface bombarded by an Ar cluster beam with a mean size of 300 atoms. The upper part was bombarded and reshaped into a very smooth region.

the Cu surface (upper portion of Fig. 34) is reshaped into a very smooth region. This surface smoothing was accomplished even though the energy-per-atom value in the cluster beam was only 100 eV. One possible explanation for this effect is that those atoms ejected from the cluster in a lateral direction (lateral sputtering) during the cluster impact may be especially effective in producing a rearrangement and enhanced migration of atoms on the surface of the target, while introducing relatively little damage to the bulk of the target.

The sputtering yield has been measured for Ar cluster ion beams. A preliminary estimation shows that the yield per Ar cluster is more than 100 times the value for monomer ions.[67,68]

Gas-cluster bombardment can be summarized as follows: a new area for the ion beam modification of surfaces is being explored using clusters of gas atoms. Because of the low energy-per-atom value (a few eV) in such clusters, several new applications are feasible such as surface smoothing, surface cleaning, enhanced chemical reactivity and shallow implantation. Early results have shown that mean cluster sizes of 10^2–10^3 atoms are attained for adiabatic expansion of CO_2 gas through a small nozzle at room temperature. Bombardment of Si substrate by a CO_2 cluster beam, with clusters of 500 molecules or more, causes almost no change in the index of refraction, indicating very little surface damage. Similar experiments with Ar clusters showed that Cu surfaces became very smooth due to the cluster bombardment, probably because of marked lateral sputtering effects.

7. Conclusions

ICB methods have been reviewed from the viewpoint of physics and technology. ICB deposition has previously been applied successfully for high-quality thin-film formation of a wide variety of materials. In many cases, deposited films were markedly superior to films deposited using other conventional methods.

Clusters consisting of a large number of atoms can be formed by the supersonic expansion of vapors of materials which are either in the solid or gaseous state at room temperature. In spite of the considerable effort expended in both theoretical discussion and experiment, many questions remain with respect to cluster formation processes, cluster stability and cluster size distribution. The uncertainties in the effects of ionization techniques on cluster stability and the difficulties of detection of low-energy clusters have halted many attempts to obtain a consistent view of even so basic a question as the mass ratio of large clusters to monomer atoms. It is also quite possible that the characteristics of cluster beams depend, in subtle and complex ways, on the details of the cluster source system. The high internal temperatures calculated for condensed clusters suggest that clusters are molten and likely to be quite sensitive to collisional events with background gases, electrons and photons. Much work remains to be done before these issues can be understood.

On the technological side, it is clear that the introduction of clusters containing large numbers of atoms to a deposition beam dramatically alters the nucleation and growth of thin films and produces films with superior characteristics compared with those deposited by evaporation or sputtering techniques. Atomic-scale observations have indicated the presence of islands at the earliest stages of film deposition for ICB sources. This suggests that the formation of "instant islands" resulting from the impingement of large atomic clusters fundamentally alters the film growth paths. Additional important factors include the roles of monomer self-ions on surface reconstruction and the characteristics of the neutral atomic flux. The interplay of this complex flux of atoms and ions at the surface of a film grown by ICB deposition is certainly far more complicated than that which our existing models describe.

A gas-cluster beam system has been developed, and the interaction between accelerated gas-cluster ions and surfaces has been discussed. The system offers many possibilities for new and advanced applications in the surface processing of materials. For example, gas-cluster beams can be used in sputtering and chemical etching of the substrate, in hypershallow junction formation, in cluster-activated chemical deposition, in annealing, and in many more applications.

Acknowledgment

The authors wish to express great respect for and gratitude to Professor Emeritus T. Takagi for his support in the ICB project and related ion beam engineering research, conducted over many years at Kyoto University under his supervision. Without his foresight and leadership, this project would not have been successful. The authors wish to acknowledge the contributions of Assistant Professor H. Usui and Professor K. Matsubara who were former members of our research laboratory. Dr. Inokawa is given special recognition for his contributions to the epitaxial Al film project during his Ph.D. study. We also wish to acknowledge the contribution of the other students who have studied in our laboratory over the years.

Our ICB research has been supported by a number of visiting professors. We are grateful to Dr. M. Current (Applied Materials), Dr. M. Sosnowski (NJIT), Professor L. L. Levenson (Univ. of Colorado), Professor R. Hummel (Univ. of Florida) and Dr. Gspann (Karlsruhe). We wish to thank Professor M. Swanson for valuable discussion and for suggestions in improving the manuscript, as well as for contribution to the ICB program.

Dr. W. L. Brown (Bell Labs.), Professor J. W. Mayer (Cornel Univ.), Professor F. Saris (FOM) and the late G. D. Stein (North-western Univ.) have provided opportunities to work in their laboratories on studies related to ICB. Dr. K. H. Westmacott and Dr. U. Dhamen of the National Center for Electron Microscopy at LBL collaborated in the electron microscope experiments. A number of our students who visited there appreciated their kind assistance in these experiments. Their stimulation and suggestions have been most helpful. From the industrial side, the ICB work has been supported

by the transfer of our original research into practical applications. We are especially grateful to Dr. P. Rose and Dr. P. Younger (Eaton), Mr. A. Kirkpatrick (Epion), Dr. S. Yasunaga (Mitsubishi) and Dr. K. Matsuda (Nissin) for their contributions.

Funds from a Grant-in-Aid for Scientific Research from the Ministry of Education, Science and Culture have greatly supported this large and long-term experimental study and made possible the transfer of these ideas to the industrial side. Special funding from the Kyoto University Engineering Department is also appreciated. Finally, we would like to express our appreciation to many others who have supported our ICB work and whom we are not able to cite in this acknowledgment.

1) A. Kantrowitz and J. Grey: Rev. Sci. Instrum. **22** (1951) 328.
2) E. W. Becker, K. Bier and W. Henkes: Z. Phys. **146** (1956) 333.
3) W. Henkes: Z. Naturforsch. a **17** (1962) 786.
4) M. A. Duncan and D. H. Rouvray: Sci. Am. (1989) 110.
5) T. Takagi, I. Yamada, M. Kunori and S. Kobiyama: *Proc. 2nd Int. Conf. Ion Sources, Vienna, 1972* (Österreichishe Studiengessellschaft für Atomenergie, Vienna, 1972) p. 790.
6) *Physics and Chemistry of Finite Systems: From Clusters to Crystals*, eds. P. Jena, S. N. Khanna and B. K. Rao (Kluwer Academic Publishers, Amsterdam, 1992).
7) I. Yamada, H. Inokawa and T. Takagi: J. Appl. Phys. **56** (1984) 2746.
8) I. Yamada: Physica Scr. **T35** (1991) 245.
9) I. Yamada, C. J. Palmstrøm, E. Kennedy, J. W. Mayer, H. Inokawa and T. Takagi: Mater. Res. Soc. Symp. Proc. **37** (1984) 1227.
10) I. Yamada, G. H. Takaoka, H. Usui, F. Satoh, Y. Itoh, K. Yamashita, S. Kitamoto, Y. Namba, Y. Hashimoto, Y. Maeyama and K. Machida: Nucl. Instrum. & Methods Phys. Res. B **59/60** (1991) 216.
11) M. Adachi, S. Ikuni, K. Yamada, H. Usui and I. Yamada: Nucl. Instrum. & Methods Phys. Res. B **59/60** (1991) 940.
12) I. Yamada, G. H. Takaoka, M. I. Current, Y. Yamashita and M. Ishii: to be published in Nucl. Inst. Methods Phys. Res. (1992).
13) I. Yamada, T. Takagi, R. P. Younger and J. Blake: Proc. SPIE **530** (1985) 75.
14) J. B. Anderson: *Molecular Beams and Low Density Gasdynamics*, ed. P. R. Wegner (Marcel Dekker, New York, 1974) Chap. 1.
15) G. D. Stein: *Proc. Int. Ion Engineering Congr. Kyoto, 1983* (Institute of Electrical Engineering of Japan, Tokyo, 1983) Vol. 2, p. 1165.
16) *CRC Handbook of Chemistry and Physics*, ed. R. C. Weast (CRC Press, Inc., Florida, 1986) p. F-21.
17) I. Yamada: *Proc. Int. Ion Engineering Congr. Kyoto, 1983* (Institute of Electrical Engineering of Japan, Tokyo, 1983) Vol. 2, p. 1177.
18) J. Frenkel: *Kinetic Theory of Liquids* (Dover, New York, 1955).
19) W. Thomson: Proc. R. Soc. Edinburgh **7** (1870) p. 63.
20) Facom Fortran SSL II User's Guide, Fujitsu, Tokyo, 1981, p. 459.
21) A. W. Searcy, R. D. Freeman and M. C. Michel: J. Am. Chem. Soc. **76** (1954) 4050.
22) W. Knauer: J. Appl. Phys. **62** (1987) 841.
23) M. Sosnowski, S. Krommenhoek, J. Sheen and R. H. Cornely: J. Vac. Sci. Technol. A **8** (1990) 1458.
24) T. Takagi: Vacuum **36** (1986) 22.
25) A. Ueda, H. Usui, I. Yamada and T. Takagi: *Proc. 9th Symp. Ion Sources and Ion-Assisted Technology, Tokyo, 1985* (Research Group of Ion Engineering, Kyoto University, Kyoto, 1985) p. 45.
26) J. G. Pruett, H. Windishmann, M. L. Nicholas and P. S. Lampard: J. Appl. Phys. **64** (1988) 2271.
27) D. E. Turner, K. M. Lakin and H. R. Shanks: Mater. Res. Soc. Proc. **128** (1989) 125.
28) J. Gspann: Nucl. Instrum. & Methods Phys. Res. B **37/38** (1989) 775.
29) W. L. Brown, M. F. Jarrold, R. L. McEachern, M. Sosnowski, G. Takaoka, H. Usui and I. Yamada: Nucl. Instrum. & Methods Phys. Res. B **59/60** (1991) 182.
30) H. Usui, M. Tanaka, I. Yamada and T. Takagi: Nucl. Instrum. & Methods Phys. Res. B **37/38** (1989) 886.
31) J. Gspann: Z. Phys. D **3** (1986) 43.
32) I. Yamada, G. H. Takaoka, H. Usui and S. K. Koh: Mater. Res. Soc. Proc. **206** (1991) p. 383.
33) I. Yamada, T. Yamada, G. H. Takaoka, H. Usui, and M. I. Current: Mater. Res. Soc. Proc. **235** (1992) p. 597.
34) S. S. Kim: Ph.D. Thesis, Technological Institute, Northwestern University, Evanston, IL, U.S.A. (1981).
35) L. L. Levenson, H. Usui, I. Yamada, T. Takagi and A. B. Swartzlander: J. Vac. Sci. Technol. A **7** (1989) 1206.
36) L. L. Levenson, A. B. Swartslander, A. Yahashi, H. Usui and I. Yamada: J. Vac. Sci. Technol. A **8** (1990) 1447.
37) H. Hsieh and R. S. Averback: Phys. Rec. B **45** (1992) 4417.
38) Y. Yamamura, I. Yamada and T. Takagi: Nucl. Instrum. & Methods Phys. Res. B **37/38** (1989) 902.
39) K. H. Müller: J. Appl. Phys. **61** (1987) 2516.
40) I. Yamada, H. Usui, H. Harumoto and T. Takagi: Mater. Res. Soc. Symp. Proc. **101** (1988) 195.
41) A. Hiraki: Surf. Sci. **168** (1986) 74.
42) L. Braicovich, C. M. Garner, P. R. Skeath, C. Y. Su, P. W. Chye, I. Lindau and W. E. Spicer: Phys. Rev. B **20** (1979) 5131.
43) I. Yamada: Nucl. Instrum. & Methods Phys. Res. B **37/38** (1989) 770.
44) A. J. Learn: J. Electrochem. Soc. **123** (1976) 894.
45) U. Dahmen, J. Douin, C. J. D. Hetherington and K. H. Westmacott: presented at MRS Fall Meeting, 28 Nov. 3 Dec., 1988, Boston, U.S.A. Paper No. R3.6.
46) U. Dahmen and K. H. Westmacott: *Proc. Special Semin. Ionized Cluster Beam Technology and Its Application*, part of 13th Symp. Ion Sources and Ion-Assisted Technology, Tokyo, 1990 (The Ion Engineering Society Japan, Tokyo, 1990) p. 53.
47) T. M. Lu, P. Bai and A. S. Yapsir: Phys. Rev. B **38** (1989) 9584.
48) K. Aizawa, H. Okabayashi and A. Tanikawa: Symp. Rec. Semiconductor and Integrated Circuits Technology (1989) Vol. 37, p. 85 [in Japanese].
49) T. Kobayashi, A. Sekiguchi, N. Hosokawa and T. Asamaki: Mater. Res. Soc. Symp. Proc. **131** (1989) 363.
50) T. Ohmi, H. Kuwabata, T. Shibata, N. Kowata and K. Sugiyama: *Proc. 5th Int. VLSI Multilevel Interconnection Conf. Santa Clara* (Institute of Electrical and Electronics Engineers, New York, 1988) p. 446.
51) T. Thangaraj, J. Reyes-Gasga, K. H. Westmacott and U. Dahmen: Mater. Res. Soc. Symp. Proc. **221** (1991) 87.
52) T. Takagi: Oyo Buturi **55** (1986) 746 [in Japanese].
53) I. Yamada: *Proc. Special Semin. Ionized Cluster Beam Technology and Its Applications*, at 13th Symposium on Ion Sources and Ion-Assisted Technology Tokyo, 1990 (The Ion Engineering Society Japan, Tokyo, 1990) p. 1.
54) I. Yamada and T. Takagi: IEEE Trans. Electron Devices **ED-34** (1987) 1018.
55) T. M. Reith and J. D. Schick: Appl. Phys. Lett. **25** (1974) 524.
56) I. Yamada, H. Usui and R. E. Hummel: *Proc. 1st Int. Symp. Advanced Materials for ULSI* (Electrochemical Society, Pennington, NJ, 1988) Vol. 88-19, p. 217.
57) K. Shiojima and T. Okumura: Jpn. J. Appl. Phys. **30** (1991) 2127.
58) W. Mönch: Phy. Rev. Lett. **58** (1987) 1260.
59) L. G. Darratt: Phy. Rev. **95** (1954) 359.
60) Y. Kawagoe, K. Yamanishi, K. Imada and K. Sato: Nucl. Instrum. & Methods Phys. Res. B **59/60** (1991) 1426.

61) M. Shinohara, F. Ohtani, O. Ishiyama and M. Asari: Mater. Res. Soc. Symp. Proc. **221** (1991) 423.
62) H. Hirayama, G. H. Takaoka, H. Usui and I. Yamada: Nucl. In strum & Methods Phys. Res. B **59/60** (1991) 207.
63) K. Fukushima and I. Yamada: to be published in Proc. 7th Int. Conf. Surface Modification of Metals by Ion Beams, Washington D.C. (Elsevier Science, Amsterdam).
64) H. Usui, I. Yamada and T. Takagi: J. Vac. Sci. Technol. A **4** (1986) 52.
65) I. Yamada, H. Usui, A. Yamada and H. Sugiyama: Nucl. Instrum. & Methods Phys. Res. B **59/60** (1991) 219.
66) I. Yamada: Oyo Buturi **60** (1991) 718 [in Japanese].
67) J. A. Northby, T. Jiang, G. H. Takaoka, I. Yamada, W. L. Brown and M. Sosnowski: to be published in Nucl. Inst. Methods Phys. Res. (1993).
68) I. Yamada, W. L. Brown, J. A. Norhby and M. Sosnowski: to be published in Nucl. Inst. Methods Phys. Res. (1993).